A Cubic Wireless Charging Container System With Highly Uniform Magnetic Field Distribution

Kaiyuan Wang, *Student Member, IEEE*, Zhen Sun, *Student Member, IEEE*, Xinze Li, *Member, IEEE*, Yao Wang, *Member, IEEE*, and Yun Yang, *Senior Member, IEEE*

***Abstract*—This article introduces a spatial wireless charging system featuring a cubic transmitter (Tx) designed for strong and uniform magnetic field distribution inside the Tx container. The Tx coils are wound with two separate wires on the exterior surfaces of the container, employing a decoupled structure. The rotational current control method is employed for the Tx resonators along the *x*- and *y*-axes to improve the uniformity of the magnetic field distribution. Within the container, planar receiver coils can achieve consistent charging with stable received voltage and maximum efficiency, regardless of the movement along the *x*- or *y*-axis, self-rotation at various positions, or revolution around the central point of the container. Practical results confirm that the proposed design exhibits smaller deviations in output voltage and overall efficiency (from dc to dc) compared to the conventional design for spatial wireless power transfer systems operating at 200 kHz and 401 kHz across the four different scenarios.**

***Index Terms*—Maximum efficiency, output deviations, spatial wireless power transfer (WPT), transmitter (Tx) coil design, uniform magnetic field distribution.**

I. Introduction

WIRELESS power transfer (WPT) is an emerging technology enabling the wireless transmission of electric power across various applications [1]. In numerous electrical devices, including portable devices [2], biomedical implants [3], and industrial robots [4], the positions and orientations often change during the charging process. Traditional planar WPT systems face considerable challenges in maintaining stable output due to lateral and angular misalignment of the receiver (Rx). This instability severely restricts their practical applications.

Various omnidirectional WPT technologies have been developed to enhance free-positioning capabilities and accommodate arbitrary orientations. Among these technologies, the foundational components are the designs of electromagnetic couplers, which include transmitter (Tx) and Rx coils. A typical Tx coil, which can be circular [5] or square [6] in shape, is arranged in an orthogonal configuration. To create a rotating magnetic field that enables three-dimensional (3-D) WPT, the amplitude, frequency, or phase of the excitation currents in the Tx coils are precisely controlled [7]. In specific situations, such as when the Rx coil is vertically oriented, the Tx coils need only generate magnetic flux horizontally. This simplifies the 3-D WPT system, effectively reducing it to a 2-D configuration [8].

In addition to traditional orthogonal coils, various types of Tx coils have been proposed to meet diverse requirements, including bowl-shaped [9], [10], tubular-shaped [11], [12], octagonal prisms [13], [14], and cubic structures [18], [19], [20], [26], [27], [28], [29], [30], [31], [32], [33], among others. The cubic configuration stands out due to its straightforward manufacturing process and suitability for practical installations. The primary objective of these coils is to ensure sufficient and uniform distribution of the magnetic field. For instance, power electronic equipment, mandated by the international thermonuclear experimental reactor (ITER) organization, must undergo testing in a stable magnetic field to verify magnetic field immunity [15], [16]. Moreover, the cubic structure is recommended for such magnetic field immunity assessments by both the ITER organization and the International Electrotechnical Commission [17].

Various coil designs for cubic structures have been explored with Rx positioned both outside [18], [19], [20] and inside the Tx [26], [27], [28], [29], [30], [31], [32], [33]. In [18], a cubic Tx is created by wrapping a single turn of copper wire around its edges, which performs well when the Rx coil rotates around it but does not support self-rotation of the Rx coil. In [19], twelve magnetic dipole coils with specific current directions are used to achieve a uniform magnetic field distribution for a multiload power supply. In [20], the Tx design mirrors that of [19], with the Rx comprising two dipole coils aimed at maximizing magnetic flux reception from the Tx. However, these designs are constrained in practical applications due to their high material costs and weight. Moreover, the output performance is significantly affected by the distance between the Rx and Tx.

For Rx inside the cubic Tx, the Helmholtz coil structure, particularly the square configuration, has gained attention for its simple design and ability to provide highly uniform magnetic fields [21], [22]. Square Helmholtz coils offer a larger accessible volume compared to round ones [23], with slightly superior uniformity of the magnetic field at the center [24]. However, conventional Helmholtz coils face challenges in cubic Tx due

Received 5 July 2024; revised 2 October 2024; accepted 31 October 2024. Date of publication 4 November 2024; date of current version 26 December 2024. This work was supported in part by A*Star MTC Young Individual Research Grant (YIRG) under Grant M23M7c0115 and in part by the Ministry of Education (MoE) Academic Research Fund (AcRF) Tier-1 under Grant RG134/23. Recommended for publication by Associate Editor K. Park. *(Corresponding author: Yun Yang.)*

Kaiyuan Wang, Zhen Sun, Yao Wang, and Yun Yang are with the Nanyang Technological University , Singapore 639673 (e-mail: kaiyuan002@e.ntu.edu.sg; SUNZ0028@e.ntu.edu.sg; yao.wang@ntu.edu.sg; yun.yang@ntu.edu.sg).

Xinze Li is with the University of Arkansas, Fayetteville, AR 72701 USA (e-mail: xinzel@uark.edu).

Color versions of one or more figures in this article are available at https://doi.org/10.1109/TPEL.2024.3491072.

Digital Object Identifier 10.1109/TPEL.2024.3491072

to space constraints. For round Helmholtz coils, the coils must be spaced at their radius, while for square ones, the spacing should be 0.545 times the coil diameter [25]. Addressing this, Basar et al. [26], Deng et al. [27], and Huang et al. [28] utilized multi-Helmholtz coils, yet these generate magnetic fields in only one direction, limiting true omnidirectional wireless charging unless coils are wound around all surfaces, which restricts access to and removal of the Rx from the container. In [29] and [30], folded coil designs are proposed, offering more flexible charging space and improving the uniformity of magnetic field distribution. However, these designs maintain a fixed excitation current direction, resulting in a magnetic field vector in one direction and lacking true omnidirectional 2-D magnetic fields. A comparison of magnetic field distributions in a cubic Tx is detailed in [31], examining scenarios with both identical and nonidentical excitation currents. Results indicate that nonidentical excitation currents yield a more homogeneous magnetic field distribution. In [32] and [33], nonidentical current control schemes are implemented in cubic-type Tx. In [32], dual sets of square coils are employed with a phase difference angle approaching 90° to mitigate cross-coupling effects. In [33], two pairs of circular Tx coils are utilized, and system efficiency is optimized by adjusting the excitation current amplitudes. However, the coil configurations in [32] and [33] fall short of achieving optimal performance, resulting in nonuniform magnetic field distributions within the cubic space.

This article introduces a novel Tx coil design tailored for a cubic container. A meta-heuristic algorithm is applied to search for the optimal parameters for the proposed Tx, while a Pareto frontier is presented to illustrate their interdependencies. Compared to conventional cubic Tx designs, the proposed approach achieves enhanced magnetic field distribution strength and uniformity, ensuring stable output voltage and maximum efficiency. Additionally, a thorough circuit analysis of the cubic WPT system, focusing on current phase difference modulation, is conducted. This analysis evaluates key metrics such as output voltage, maximum efficiency, and the impact of Tx cross coupling.

The main contributions of this article can be summarized as follows.

1) A novel cubic Tx capable of generating a homogeneous magnetic field is proposed for the first time, and its optimal parameters are determined using a meta-heuristic algorithm.
2) Pareto frontiers are used to clearly illustrate the relationships between wire length, magnetic flux density, and field distribution uniformity in the proposed Tx.
3) A comprehensive circuit analysis is performed for the proposed Tx, followed by the development of a prototype spatial WPT system that ensures stable output voltage and maximizes efficiency.

II. Previous Research on Cubic Wireless Charging Containers

Based on the placement of Rx, cubic WPT Tx designs can be categorized into two types: 1) where the Rx is positioned outside the Tx [18], [19], [20], and 2) where the Rx is situated inside the Tx [26], [27], [28], [29], [30], [31], [32], [33]. For the latter type, a typical Tx structure, referred to as Design-1, is illustrated in Fig. 1(a). This design employs two pairs of coaxial rectangular coils within a cubic space characterized by dimensions d (length, width, and height). Both x-axis coils (x_1 and x_2) and y-axis coils (y_1 and y_2) are connected in series, sharing identical currents. While this configuration may derive from square Helmholtz coils [see depicted in Fig. 1(b)] [34], the coil placements are adjusted to the edges of the cubic container, enhancing flexibility in charging spatial arrangements. A Helmholtz coil consists of two parallel coaxial coils that generate a uniform magnetic field in one direction within a specific region. To achieve magnetic fields in multiple directions, configurations with two [34] or three [35] sets of orthogonal Helmholtz coils are used. However, Helmholtz coils have two main limitations. First, they only ensure a uniform magnetic field between the coil pair, with significant degradation of uniformity outside this region [36]. Second, the close proximity between coil pairs poses challenges for practical installation due to high space occupation [37]. Although Fig. 1(a) offers more charging space compared to Fig. 1(b), it compromises the uniformity of the magnetic field within the coils [36]. To achieve uniform magnetic fields over larger areas, designs with configurations of three [28], [38], four [38], or five [39] square-coil sets have been proposed. However, these multisquare coil designs generate magnetic fields in only one direction. For magnetic fields in multiple directions, coils would need to be wound around all surfaces of the cubic container, limiting practical access and removal of the Rx. Therefore, considering space efficiency, the coil configuration depicted in Fig. 1(a) is adopted here as the conventional design for cubic-type Tx [29], [30], [31], [32], [33].

Inside the container, a magnetic field can be either nonrotational or rotational depending on the use of nonidentical current

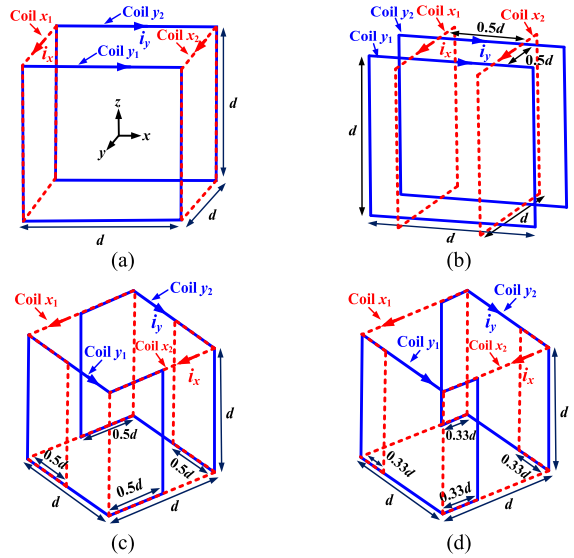

Fig. 1. Three-dimensional view of the existing cubic-type Tx designs for the Rx placed inside the Tx. (a) Conventional design (Design-1). (b) Square Helmholtz coils. (c) Folded coil design with 50% folded ratio. (d) Improved folded coil design with 33% folded ratio.

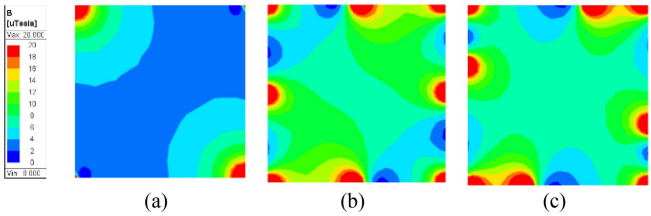

Fig. 2. Top view of the magnetic field distribution for (a) Design-1, (b) folded coil design with 50% folded ratio, and (c) improved folded coil design with 33% folded ratio.

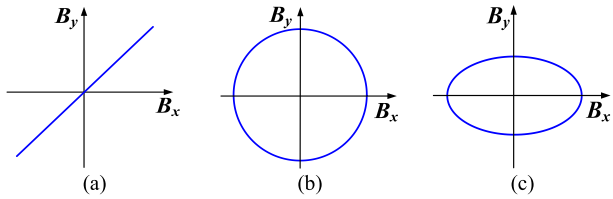

Fig. 3. Magnetic field trajectory for (a) zero phase difference between B_x and B_y and $B_x = B_y$; (b) 90-degree phase difference between B_x and B_y and $B_x = B_y$; (c) 90-degree phase difference between B_x and B_y and $B_x = 2B_y$.

modulation [7]. Achieving a nonrotational magnetic field is simpler as it requires only one inverter without the need for any current control methodologies. For Design-1, a straightforward method to generate a nonrotational magnetic field is by connecting coil x and coil y in series. The magnetic field distribution is simulated using the finite element method (FEM) software Ansys Maxwell, version 2023 R1. In the simulation, the dimension d is set to 200 mm, as this size is appropriate for wearable consumer electronics and implantable medical devices [18], [32]. The coil consists of a single turn, with an excitation current amplitude set to 1 A. Based on the current flow directions shown in Fig. 1(a), Fig. 2(a) illustrates the top-view magnetic field distribution for the layer positioned at a height of $d/2$. The magnetic field distribution exhibits nonuniformity, characterized by concentrated strong magnetic fields at two corners. This phenomenon arises from the codirectional currents in coils x and y at these corners. Conversely, weaker magnetic fields are observed at the remaining corners, where opposing current directions in the coils result in diminished magnetic flux density. To mitigate this issue, the concept of a folded coil design was initially introduced in [29]. This design, depicted in Fig. 1(c), replaces the rectangular coils of Design-1 with L-shaped coils. In this configuration, the terminal wire is folded towards the midpoint of adjacent edges, utilizing a fixed 50% folding ratio to facilitate construction. Similar to Design-1, both x-axis coils (x_1 and x_2) and y-axis coils (y_1 and y_2) are connected in series, ensuring identical currents. This design prevents flux cancellation or enhancement at the four corners, resulting in a stronger and more uniform flux distribution compared to Design-1. The top view of the magnetic field distribution for this design is shown in Fig. 2(b). In [30], the folding ratio was optimized to 33% [as shown in Fig. 1(d)] by manually adjusting it from 5% to 95%. This optimization further improves the uniformity of the magnetic field distribution, as demonstrated in the simulated results presented in Fig. 2(c).

While the designs in [29] and [30] achieve a more uniform magnetic field distribution than Design-1, their nonrotational magnetic fields do not support true 2-D WPT because the main magnetic field vector sum points in a specific direction. Denoting the magnetic flux density amplitudes in the x-axis and y-axis directions as B_x and B_y, respectively, the magnetic field trajectory when B_x equals B_y forms a 45° line, as illustrated in Fig. 3(a). This linear trajectory restricts energy transfer to a single direction, making it challenging for the Rx coil positioned parallel to this line to capture energy effectively. To achieve true 2-D WPT, a straightforward approach is to introduce a 90-degree phase difference between the two excitation currents, i_x and i_y. This causes B_x and B_y to vary over time. When B_x equals B_y, the magnetic field trajectory over one cycle becomes circular, as depicted in Fig. 3(b). This circular trajectory enables the magnetic field direction to change continuously, ensuring stable energy transfer regardless of the Rx coil's orientation. However, if B_x equals $2B_y$, the magnetic field trajectory over one cycle becomes elliptical, as shown in Fig. 3(c). Although the elliptical trajectory also allows the magnetic field direction to vary over time, the unequal magnitudes in different directions lead to uneven energy capture by the Rx at different orientations. This results in output fluctuations when the Rx rotates.

Compared to [29], this article introduces a novel spatial coil structure by analyzing the magnetic field characteristics in a cubic space. A specific coil optimization process is presented, detailing the relationship among wire length, magnetic flux density, and field uniformity, leading to the identification of the most suitable coil parameters. Besides, a nonidentical current control scheme, rather than the identical current control scheme in [29], is employed to implement true 2-D spatial WPT. The coupling between the Tx coils and the system analysis based on the nonidentical control scheme are also thoroughly discussed.

III. Coil Design of the Proposed System

A. Magnetic Field Distribution for Conventional Design-1

Given the symmetry between the coils in the x-axis and y-axis directions, the magnetic flux density generated by coil y exemplifies the performance of Design-1. In the simulation, dimension d is set to 200 mm, with the coil consisting of a single turn and an excitation current amplitude of 5 A. Due to the symmetric nature of the magnetic field along the z-axis, Fig. 4 illustrates the top-view magnitudes of the magnetic flux density for three layers along the positive z-axis.

As shown in Fig. 4, the magnetic field distribution exhibits nonuniformity due to magnetic flux cancellation between coils y_1 and y_2 in the conventional coil design, resulting in a weakened magnetic field in both the central and near-edge regions. Therefore, optimizing the geometry of the Tx coils is crucial to achieving a uniform magnetic field distribution, which will be further discussed in the following section.

B. Proposed Coil Design-2

Design-2 (see Fig. 5) differs from Design-1 in that it features multiple folded coils arranged in a U-shape around the side

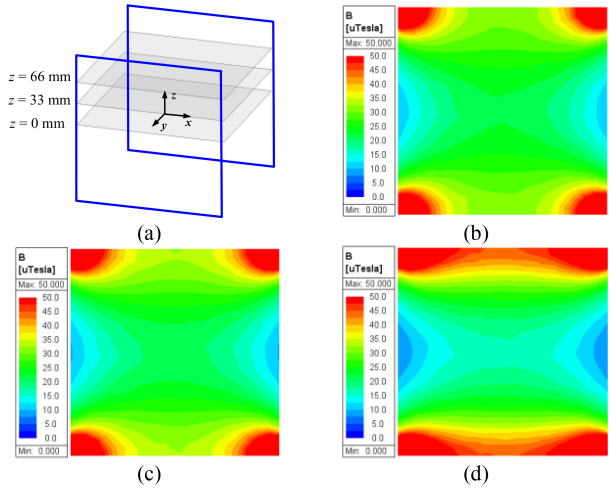

Fig. 4. (a) Schematic diagram of the coil y in Design-1 and the testing layers. (b), (c) Magnitude of the magnetic flux density of each layer, i.e., (b) $z = 0$ mm, (c) $z = 33$ mm, and (d) $z = 66$ mm.

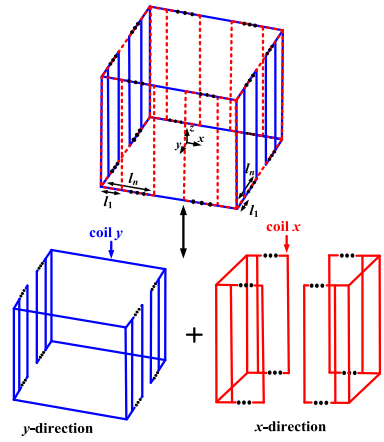

Fig. 5. Three-dimensional view of the proposed coil design.

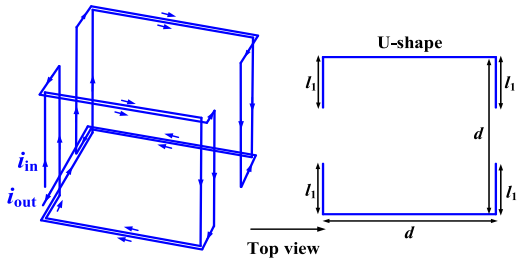

Fig. 6. Schematic diagram for general winding of the proposed coil in the y-axis direction.

surfaces (see Fig. 6). The proposed design combines folded coil concepts from [29], [30] with multiple-square coil designs from [38] to [39]. In contrast to previous iterations, this design optimizes space utilization by winding coils around the four faces of the cubic container parallel to the z-axis, leaving the top and bottom surfaces free. This configuration ensures a highly uniform magnetic field distribution within the container, allowing the magnetic field to point in any direction within the xy

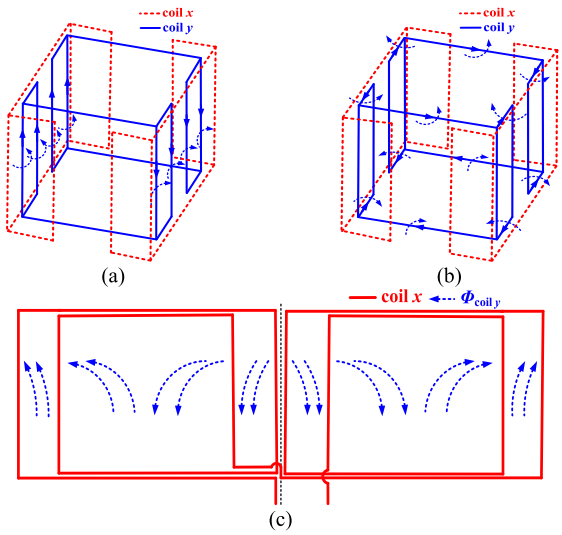

Fig. 7. Schematic diagram of the magnetic flux generated by (a) vertical wires, (b) horizontal wires, and (c) both vertical and horizontal wires of coil y.

plane. The vertical wires of the multiple folded coils mitigate flux cancellation observed in Design-1, resulting in a more uniform and robust magnetic field distribution.

The proposed coil design incorporates two sets of coils in the x- and y-directions, featuring multiple folded coils wound around adjacent faces. The number of folded coils in each face is denoted by n, and the folded length of each U-shaped coil is denoted by l_i (where $i = 1, 2, \ldots, n$), winding each set of coils with a single wire is feasible. For instance, when $n = 1$ and $l_1 = d/3$, the structure and parameters for coil y are illustrated in Fig. 6.

It is important to note that despite the overlaps of two sets of the Tx coils, the ideal coupling between them can be zero. Using the coil in Fig. 6 as an example, the magnetic flux generated by the vertical and horizontal wires for coil y is illustrated in Fig. 7(a) and (b), respectively. The dimension of coil x is slightly enlarged for clarity. Due to the designed symmetrical winding structure, the total magnetic flux generated from coil y to coil x is zero. The 3-D structure of the coil complicates the visualization of the flux distribution. To simplify the analysis, coil x is represented in 2-D form, as shown in Fig. 7(c). $\Phi_{\text{coil}\,y}$ represents the magnetic flux generated from coil y to coil x. Apparently, the net flux for coil x is zero, indicating that the two Tx coils are decoupled.

C. Coil Optimization

Due to symmetry between coil x and y, the optimization process for coil y exemplifies the methodology applied in this study. The optimization aims to achieve a strong and uniform magnetic field distribution within the cubic space. Based on the coil structure in Fig. 5, two key optimization parameters are considered: the number of folded coils (denoted as n) and the length of each folded coil (l_i for i from 1 to n, where l_i can vary for each fold). The optimization settings for the proposed design are summarized in Table I and discussed below. To achieve a uniform

TABLE I
CONFIGURATIONS OF THE OPTIMIZATION

Terms	Specifications
Coil parameters	Number of folds $n \in [1, 4]$ Length of each fold $l_i \in [5\text{ mm}, 95\text{ mm}]$, $i = 1, \ldots, n$
Design objectives	Minimize CoV with acceptable μ and L
Simulated annealing	Initial temperature = 5230°C Factor for acceptance distribution = −5 Factor for visiting distribution = 2.62 Maximal epochs = 1500

magnetic field, the coefficient of variation (CoV), a measure of the dispersion of magnetic flux density, is minimized. CoV, also known as relative standard deviation in statistics, indicates the degree of magnetic field uniformity. A lower CoV signifies a more concentrated magnetic field with minimal dispersion. Additionally, optimizing the average magnetic flux density μ and total coil length L are considered. Reducing the coil length L can lower system costs and losses. In this study, CoV is given top priority in optimization, while ensuring μ and L remain within reasonable ranges. In summary, the optimization problem can be briefly formulated as

$$\min_{n,\, l_1,\, \ldots,\, l_n} \mathrm{CoV}\,(n, l_1, \ldots, l_n) = \frac{\sigma}{\mu} \tag{1}$$

where

$$\mu = \frac{1}{N^3} \sum_{i=1}^{N} \sum_{j=1}^{N} \sum_{k=1}^{N} B\,(x_i, y_j, z_k) \tag{2}$$

$$\sigma = \sqrt{\frac{1}{N^3} \sum_{i=1}^{N} \sum_{j=1}^{N} \sum_{k=1}^{N} \left(B\,(x_i, y_j, z_k) - \mu\right)^2}. \tag{3}$$

It is important to note that deriving an analytical solution for (1) using the Biot–Savart law is challenging due to the complex geometry of the coils and the large number of test points required for calculating the CoV. A simplified analysis process is provided in the Appendix. The magnetic field is simulated using the FEM in Ansys Maxwell. The average and CoV of the magnetic flux density inside the container are estimated based on measurements taken at 753 571 test points (91×91×91) spaced at 2 mm intervals from 10 mm to 190 mm along each dimension. To address the combinatorial optimization problem stated in (1), a simulated annealing (SA) algorithm is employed iteratively, as depicted in Fig. 8. The optimization process involves two nested algorithm loops, utilizing design automation techniques. In the outer loop of the algorithm, the number of folded coils n is enumerated, while in the inner loop, the optimal fold lengths l_i are determined using SA.

The process of SA in the inner algorithm loop proceeds as follows: First, initial candidate fold lengths are generated, and their respective objective functions, denoted as $O(\{p_i\}_{\mathrm{ini}})$ are computed. Second, a new solution is generated based on temperature conditions, and its objective function $O(\{p_i\}_{\mathrm{new}})$ is evaluated. Third, the difference ΔO between the objective value of the previous candidate fold lengths and the new ones is used to determine acceptance. If the objective value decreases, the new fold lengths are accepted; otherwise, the Metropolis rule is applied. The Metropolis rule determines whether to accept a less favorable candidate solution when the new solution does not improve the objective value [40]. According to this rule, a worse solution can still be accepted with a probability P given by

$$P = exp\left(\frac{-\Delta O}{T}\right) = exp\left(\frac{-O\left(\{l_i\}_{ini}\right) + O\left(\{l_i\}_{\mathrm{new}}\right)}{T}\right) \tag{4}$$

where T represents the temperature, which decreases over time as the algorithm progresses. During the initial iterations, when T is high, there is a greater probability of accepting worse solutions, encouraging exploration of the solution space. As the temperature decreases (annealing), the likelihood of accepting worse solutions diminishes, directing the search toward local refinement and convergence.

Finally, the temperature anneals decrease the acceptance probability in the Metropolis rule. This iterative process continues until the required number of iterations is achieved. All candidate solutions during the search process are recorded, and the Pareto frontier is evaluated to offer diverse optimal designs for various scenarios.

The optimization process of the employed algorithm is illustrated in Fig. 9. As SA iterates, the CoV improves while magnetic flux density increases. Specifically, with $n = 3$, after 220 epochs, the algorithm gradually converges, transitioning from global optimization to local exploitation. For the case of three-folded coils, compared to the first epoch, the design optimized for uniformity reduces CoV by 0.09 (32.5%) and enhances magnetic flux density by 3.10 μT (11.9%).

To demonstrate the superior performance of the employed algorithm, its computational efficiency is compared with the conventional brute-force grid search method, as summarized in

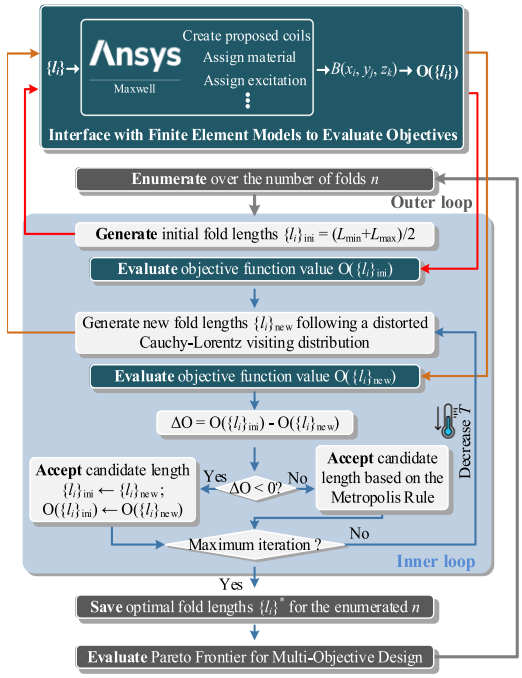

Fig. 8. Two-stage multiobjective optimization of the proposed coil design using SA algorithm.

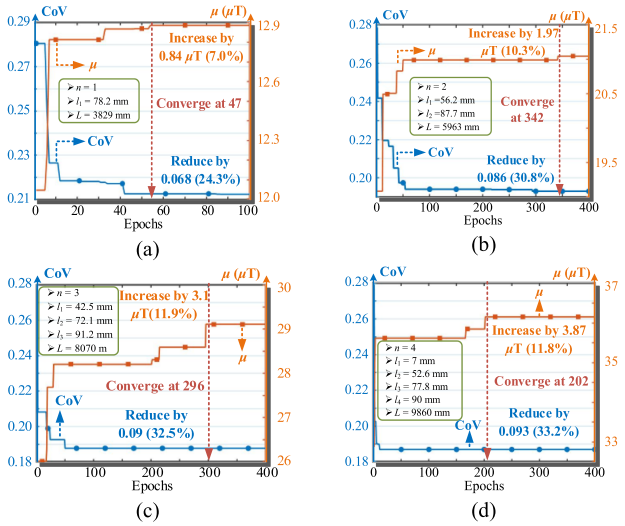

Fig. 9. Optimization trajectory of the best CoV and μ searched during iteration for (a) $n = 1$; (b) $n = 2$; (c) $n = 3$; (d) $n = 4$.

TABLE II
COMPUTATION COSTS OF SA AND GRID SEARCH

Optimization algorithm	$n = 1$	$n = 2$	$n = 3$	$n = 4$	$n = n$
Grid search ($M = 100$)	102	104	106	108	$O(M_n)$
Simulated annealing (SA)	53	342	296	202	Linear
Improvements of SA (%)	47	96.58	99.97	99.9998	-

Table II. The grid search method exhibits the curse of dimensionality, necessitating an exponential increase in FEM simulations as the number of folds n increases, specifically O(M^n), where M represents the number of partitioned values for fold length l_i. In contrast, the employed optimization algorithm requires significantly fewer FEM simulations, achieving a reduction in computational cost by 96.58% and 99.97% when $n = 2$ and $n = 3$, respectively.

The optimization results for different values of n with minimal CoV with the corresponding maximal magnetic flux density are summarized in Fig. 10(a). For $n = 0$, represented as Design-1 with no folded coils, the CoV is notably high at 0.413, and the magnetic flux density μ is low at 5.18 μT. Introducing the proposed design significantly reduces CoV and increases magnetic flux density. It is observed that increasing n to 2 and 3 results in substantial improvements, with CoV decreasing by 30.8% and 32.5%, and μ increasing by 10.3% and 11.9%, respectively. Although using $n = 4$ achieves optimal uniformity and magnetic flux density, the improvements over $n = 3$ (0.632% for CoV and 19.1% for μ) are marginal, considering a 22.2% increase in total coil length. Consequently, this study selects $n = 3$ for the number of folded coils.

Fig. 10(b) displays all candidate solutions and the Pareto frontier during the search process for $n = 3$. It is evident that on the Pareto frontier, three objectives conflict: 1) minimizing total coil length L, 2) achieving a low CoV for uniformity, and 3) maximizing average magnetic flux density μ. The selected design, highlighted on the Pareto frontier, achieves a minimal CoV of 0.188 and a strong magnetic flux density of 26.9 μT,

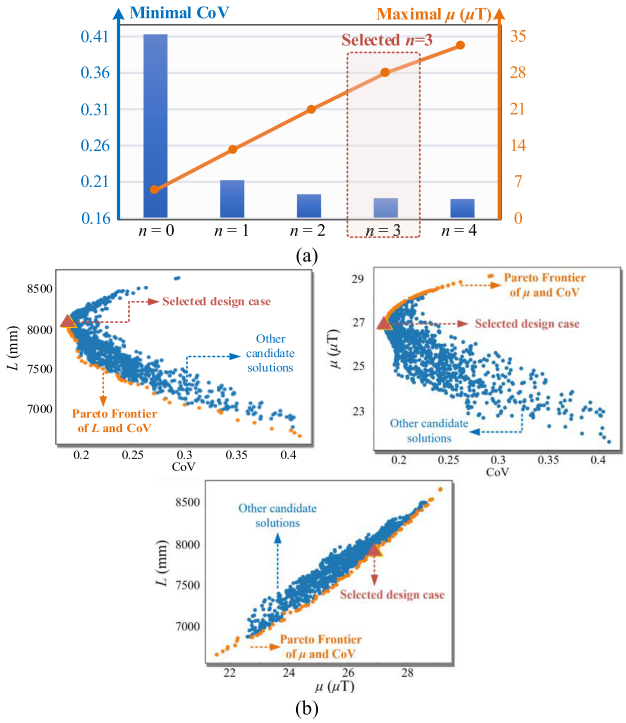

Fig. 10. Optimization results: (a) minimal CoV and the corresponding maximal μ; (b) all candidate solutions and the Pareto frontier when $n = 3$.

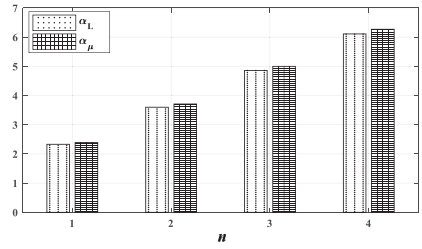

Fig. 11. Comparisons of the α_L and α_μ.

albeit at the cost of increased total coil length. Fig. 11 illustrates the ratios of L (denoted as $\alpha_L = L_{Design2}/L_{Design1}$) and μ (denoted as $\alpha_\mu = \mu_{Design2}/\mu_{Design1}$) between Design-2 and Design-1. Despite Design-2 utilizing more wires compared to Design-1, the improvement in μ Design-2 is more significant.

Fig. 12 illustrates the magnetic flux density distribution for the optimized Design-2 at three layers along the positive z-axis. The simulation conditions follow those in Fig. 4, and based on the results from Fig. 11, the coil is configured with a single turn, and the excitation current amplitude is reduced to 1 A to ensure a fair comparison.

Compared to the magnetic field distribution of Design-1 shown in Fig. 4, the proposed coil design effectively compensates for weaker areas, resulting in a more uniform magnetic field distribution. Given that coils x and y share an identical structure, the 3-D view of the optimized Design-2 is presented in Fig. 13(a)–(c). To generate a rotational magnetic field, the excitation currents for the two sets of coils are set with a 90-degree phase difference. Fig. 13(d)–(h) depict top views of the magnetic field vectors at layer $z = 0$ mm at various time

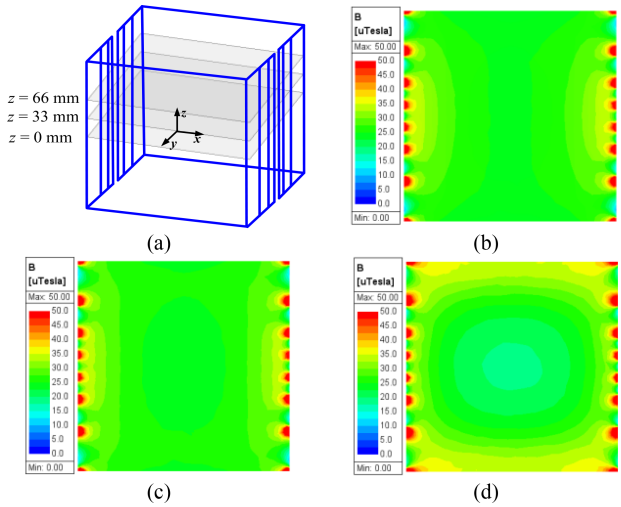

Fig. 12. (a) Schematic diagram of the proposed coil structure in y-axis direction and the testing layers. (b), (c) Magnitude of the magnetic flux density of each layer, i.e., (b) $z = 0$ mm, (c) $z = 33$ mm, and (d) $z = 66$ mm.

instants. Over time, the direction of the magnetic field rotates, and the magnitudes of the magnetic field remain nearly uniform across different time intervals.

IV. Circuit Analysis of the Proposed System

A. Analysis of the Output Voltage and Efficiency

The circuit structure of the proposed WPT system is shown in Fig. 14. The system includes two channels for the Tx circuits, each driving a respective set of Tx coils (coil x and coil y). Within each Tx circuit, *LCC* compensation is employed to generate excitation currents (i_{t1} and i_{t2}) that are independent of load and coupling conditions [41]. Series compensation is implemented in the Rx circuit to maintain a constant voltage output.

The fundamental equivalent circuit of the investigated WPT system is depicted in Fig. 15. The circuit includes high-frequency input voltages v_{p1} and v_{p2}. Components such as L_{f1}, L_{f2}, C_{f1}, C_{f2}, C_{t1}, and C_{t2} are the compensated components for the Tx. L_{t1} and L_{t2} represent the Tx coils, with R_{t1} and R_{t2} denoting their respective equivalent series resistances (ESRs). On the Rx side, L_s is the Rx coil, and C_s is its compensated capacitor, forming a series compensated network. R_s represents the ESR of L_s. R_{eq} is the equivalent load resistance of the nonlinear load, satisfying $R_{eq} = 8R_L/\pi^2$ for typical load conditions [42]. Mutual inductances M_1 and M_2 depict the coupling between the two Tx coils and the Rx coil, respectively. M_3 represents the mutual inductance between the two Tx coils.

To simplify the analysis without sacrificing generality, the inductances of the coils and the compensated capacitors in both Txs are assumed to be identical. Therefore, the system parameters can be expressed as follows:

$$\begin{cases} L_{f1} = L_{f2} = L_f\,, \quad L_{t1} = L_{t2} = L_t \\ C_{f1} = C_{f2} = C_f\,, \quad C_{t1} = C_{t2} = C_t \\ R_{t1} = R_{t2} = R_t. \end{cases} \tag{5}$$

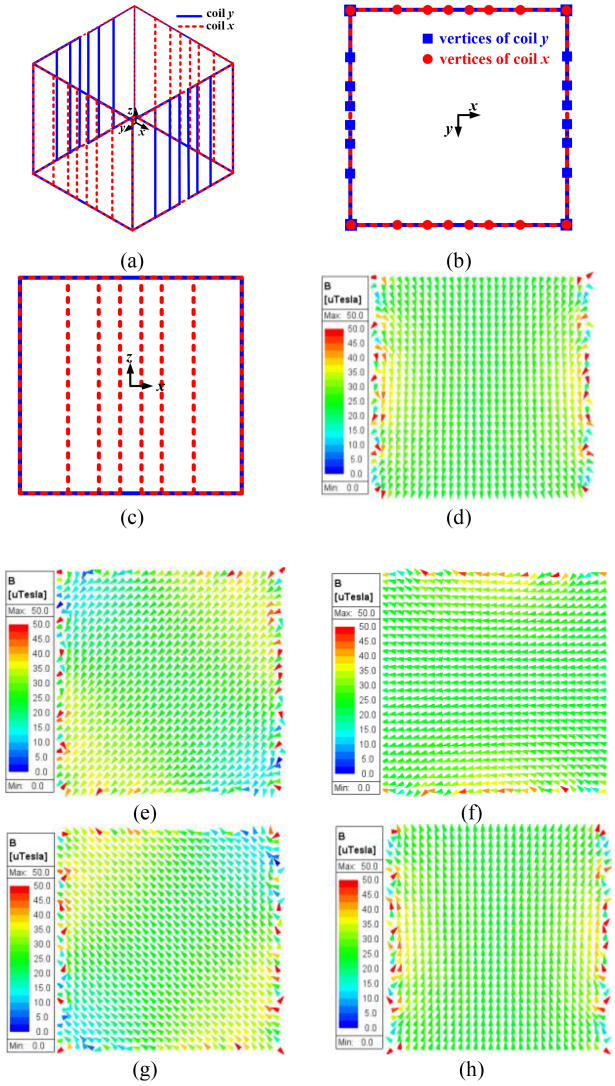

Fig. 13. (a)–(c) Schematic diagram optimized Design-2: (a) three-dimensional view, (b) view in the xy plane, and (c) view in the xz plane. (d)–(h) Vector of the magnetic field at the different time instants, i.e., (d) $\omega t = 0$; (e) $\omega t = \pi/4$; (f) $\omega t = \pi/2$; (g) $\omega t = 3\pi/4$; and (h) $\omega t = \pi$.

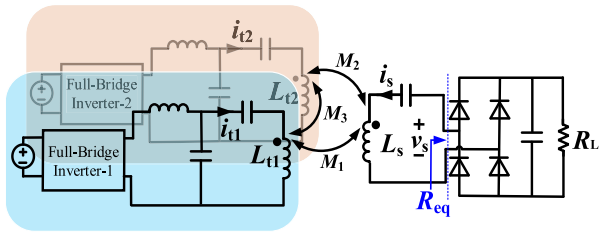

Fig. 14. Circuit diagram of the investigated system.

The capacitors are compensated at the resonant angular frequency (i.e., $\omega_o = 2\pi f_o$), which satisfies

$$\frac{1}{\sqrt{L_f C_f}} = \frac{1}{\sqrt{(L_t - L_f)\, C_t}} = \frac{1}{\sqrt{L_s C_s}} = \omega_o. \tag{6}$$

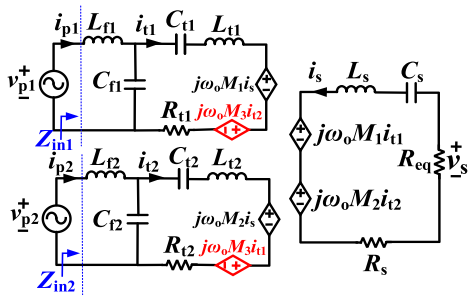

Fig. 15. Equivalent circuit of the investigated system at fundamental frequency.

Based on (5) and (6), the excitation current (i_{t1} and i_{t2}) of the Tx coils can be expressed as

$$i_{t1} = \frac{v_{p1}}{j\omega_o L_f} \tag{7.1}$$

$$i_{t2} = \frac{v_{p2}}{j\omega_o L_f}. \tag{7.2}$$

By introducing phase differences in the excitation currents among the Txs, a rotating magnetic field can be generated. In this study, a 90-degree phase difference between i_{t1} and i_{t2} is achieved by adjusting the input voltages v_{p1} and v_{p2} to satisfy

$$v_{p1} = V_p \angle 0^o \tag{8.1}$$

$$v_{p2} = V_p \angle -90^o \tag{8.2}$$

where V_p represents the root means square (rms) value of the input voltage. According to Faraday's Law, the excitation currents in the Tx coil induce controlled voltage sources in the Rx circuit, as shown in Fig. 15. Through the resonance of L_s and C_s, the voltage on the Rx side is influenced by R_{eq} and R_s. Therefore, the rms value of the output voltage can be expressed as

$$V_s = \frac{V_p M_{eq} R_{eq}}{L_f (R_s + R_{eq})} \tag{9}$$

where $M_{eq} = \sqrt{M_1^2 + M_2^2}$ represents the equivalent mutual inductance. According to (9), a constant voltage output can be achieved if R_s is ignored. However, the variations of M_{eq} are directly cause the variations of V_s. Consequently, to ensure stable output voltage, it is imperative to minimize the variation in M_{eq}. The energy transfer efficiency can be derived as

$$\eta = \frac{I_s^2 R_{eq}}{I_s^2(R_s + R_{eq}) + I_{t1}^2 R_{t1} + I_{t2}^2 R_{t2}} = \frac{R_{eq}}{R_{eq} + R_s + \frac{2R_t(R_s+R_{eq})^2}{\omega_o^2 M_{eq}^2}} \tag{10}$$

where I_s, I_{t1}, and I_{t2} are the rms values of i_s, i_{t1}, and i_{t2}, respectively. The quality factors of the coils are defined as $Q_t = \omega L_t / R_t$ and $Q_s = \omega L_s / R_s$. The equivalent coupling coefficient k_{eq} is defined as $k_{eq} = \sqrt{k_1^2 + k_2^2} = M_{eq}/\sqrt{L_t L_s}$. The ratio of the R_{eq}/R_s is denoted as γ. The efficiency in (10) can be rewritten as

$$\eta = \frac{1}{\frac{2\gamma}{k_{eq}^2 Q_t Q_s} + \frac{2+k_{eq}^2 Q_t Q_s}{k_{eq}^2 Q_t Q_s \gamma} + \frac{4+k_{eq}^2 Q_t Q_s}{k_{eq}^2 Q_t Q_s}}. \tag{11}$$

Based on (11), the maximum efficiency can be achieved by equalizing γ to

$$\gamma_{\eta max} = \sqrt{1 + \frac{k_{eq}^2 Q_t Q_s}{2}}. \tag{12}$$

By substituting (12) into (11), the maximum corresponding efficiency can be calculated as

$$\eta_{max} = \frac{k_{eq}^2 Q_t Q_s}{\left(\sqrt{2} + \sqrt{2 + k_{eq}^2 Q_t Q_s}\right)^2}. \tag{13}$$

As indicated by (13), the maximum efficiency of the system is influenced by the equivalent coupling coefficient k_{eq} and the quality factors Q_t and Q_s. Higher values of k_{eq}, Q_t, and Q_s contribute to enhancing η_{max}. For a specific WPT system with parameters detailed in Table III, the deviations of η_{max} with respect to k_{eq} and $Q_t Q_s$ are visualized in the 3-D plot shown in Fig. 16.

As depicted in Fig. 16, there is a clear increase in both k_{eq} and $Q_t Q_s$. When Q_t and Q_s are set to 400 and k_{eq} to 0.21, the maximum efficiency can reach 97.5%. It is noteworthy that variation in k_{eq} has a significant impact on η_{max}, especially when k_{eq} and $Q_t Q_s$ are low. For instance, when Q_t and Q_s are 200 and k_{eq} is 0.07, the maximum efficiency is only 81.9%.

TABLE III
MAIN PARAMETERS OF THE PROPOSED SYSTEM IN SIMULATION

Parameters	Value	Parameters	Value
L_f	8 μH	k_1	0.05–0.15
Q_t	200–400	k_2	0.05–0.15
Q_s	200–400		

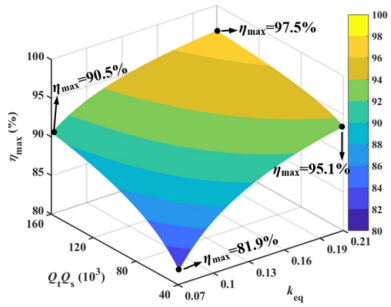

Fig. 16. Variations of η_{max} with respect to k_{eq} and $Q_t Q_s$.

B. Analysis of Cross-Coupling Effects

In the analysis mentioned earlier, cross-coupling between the two Tx coils does not affect the output voltage and efficiency due to the load- and coupling-independent excitation currents in the *LCC*-compensated networks. However, this cross-coupling could potentially exacerbate the imbalance in the input current i_{pi} (i = 1, 2) for the two Txs. As depicted in Fig. 15, the

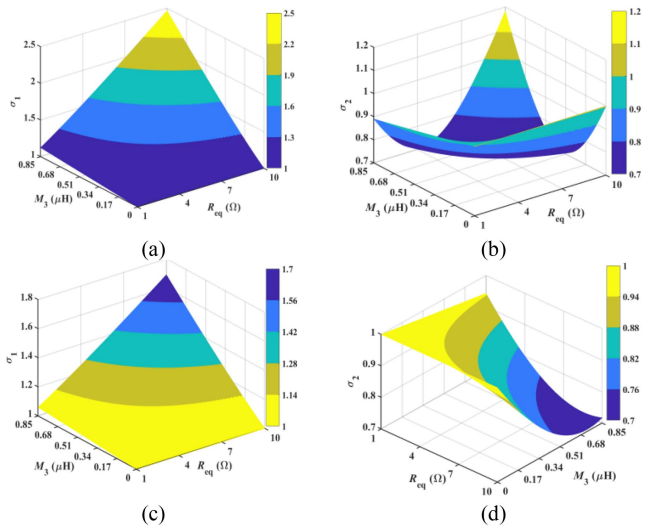

Fig. 17. Schematic diagram of the variations of σ_i with respect to M_3 and R_{eq} for (a) σ_1 with $f_0 = 200$ kHz, (b) σ_2 with $f_0 = 200$ kHz, (c) σ_1 with $f_0 = 400$ kHz, and (d) σ_2 with $f_0 = 400$ kHz.

equivalent input impedances, denoted as Z_{in1} and Z_{in2}, for each Tx can be formulated as follows:

$$\begin{cases} Z_{\text{in1}} = j\omega_o L_{\text{f1}} + \left(j\omega_o L_{\text{t1}} + \frac{1}{j\omega_o C_{\text{t1}}} + Z_{\text{ref1}} + R_{\text{t1}}\right) || \frac{1}{j\omega_o C_{\text{f1}}} \\ Z_{\text{in2}} = j\omega_o L_{\text{f2}} + \left(j\omega_o L_{\text{t2}} + \frac{1}{j\omega_o C_{\text{t2}}} + Z_{\text{ref2}} + R_{\text{t2}}\right) || \frac{1}{j\omega_o C_{\text{f2}}} \end{cases} \tag{14}$$

where Z_{ref1} and Z_{ref2} represent the reflected impedance in each Tx circuit, derived as follows:

$$\begin{cases} Z_{\text{ref1}} = \frac{j\omega_o(M_1 i_s + M_3 i_{t2})}{i_{t1}} \\ Z_{\text{ref2}} = \frac{j\omega_o(M_2 i_s + M_3 i_{t1})}{i_{t2}} \end{cases}. \tag{15}$$

To simplify the expression, the ESRs of the coils are ignored. Based on (5), (6), (7), (14), and (15), the rms value of the output current in each inverter can be expressed as

$$I_{\text{p1}} = \frac{V_{\text{p}}\sqrt{\omega_o^2 M_1^2 M_{\text{eq}}^2 + M_3 R_{\text{eq}}\left(M_3 R_{\text{eq}} + 2M_1^2\omega_o^2\right)}}{\omega_o L_{\text{f}}^2 R_{\text{eq}}} \tag{16.1}$$

$$I_{\text{p2}} = \frac{V_p\sqrt{\omega_o^2 M_2^2 M_{\text{eq}}^2 + M_3 R_{\text{eq}}\left(M_3 R_{\text{eq}} - 2M_2^2\omega_o^2\right)}}{\omega_o L_{\text{f}}^2 R_{\text{eq}}}. \tag{16.2}$$

As shown in (16), mutual inductance M_3 exacerbates the imbalance in the output currents of the two inverters. M_3 increases I_{p1}, especially when R_{eq} is large. Moreover, M_3 also increases I_{p2} if $M_3 R_{\text{eq}} > 2M_2^2\omega_o$. To qualify the influence of M_3 on I_{p}, the current imbalance ratio σ_i in relation to an ideal system is defined as follows:

$$\sigma_i = \frac{I_{\text{p}i}}{I_{\text{p}i\_\text{ideal}}} \tag{17}$$

where $I_{\text{p}i\_\text{ideal}}$ represents the ideal value of input current when $M_3 = 0$. The 3-D plot of σ_i with respect to M_3 and R_{eq}, using the parameters from Table III, is illustrated in Fig. 17. The mutual

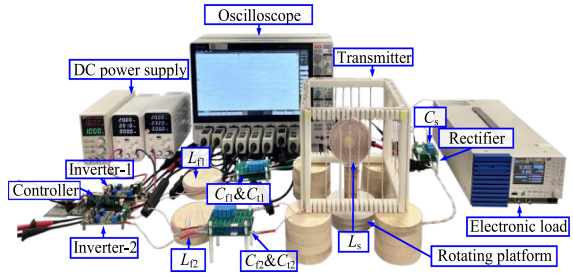

Fig. 18. Photograph of the experimental setup.

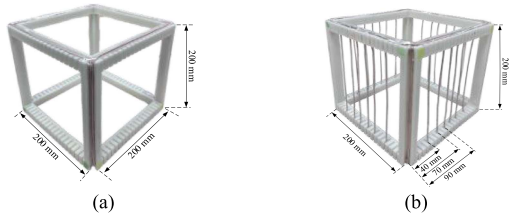

Fig. 19. Three-dimensional views of the cubic wireless charging containers based on (a) Design-1 and (b) Design-2.

inductances M_1 and M_2 are set to 2 μH, and M_3 varies from 0 μH to 0.85 μH.

As depicted Fig. 17(a), σ_1 exceeds 1 and increases with R_{eq} and M_3. A higher σ_1 implies additional current stress and increased losses in the inverter. In Fig. 17(b), σ_2 remains below 1 when R_{eq} is small. Figs. 17(c) and (d) illustrates that increasing the operating frequency reduces σ_i. However, σ_1 consistently remains above 1 for inverter-1. Therefore, cross-coupling between the two Txs exacerbates the output current imbalance. Nonetheless, as discussed in the analysis of the proposed design in Section III, strategies are in place to mitigate these cross-coupling effects.

V. Experimental Verifications

Experiments were performed using the setup illustrated in Fig. 18. Fig. 19 shows the 3-D views of the two cubic wireless charging containers (i.e., Design-1 and Design-2). For ease of construction, the lengths of each folded coil in the experiment were set as follows: $l_1 = 40$ mm, $l_2 = 70$ mm, and $l_3 = 90$ mm. These dimensions deviate slightly from the optimized simulation values of $l_1 = 42.5$ mm, $l_2 = 72.1$ mm, and $l_3 = 91.2$ mm. The simulation results showed that the average magnetic flux density μ and CoV for the experimental structure were 26.7 μT and 0.189, respectively, closely matching the optimized values of 26.9 μT and 0.188. The main parameters of the system are measured using the Wayne Kerr 6500B Electrical Impedance Analyzer, as detailed in Table IV. The self-resonant frequency of the transmitter coils is measured at 4.52 MHz, which is significantly higher than the operating frequencies of the systems. Therefore, the effects of parasitic capacitance on the Q factors are negligible. Moreover, M_3 for Design-2 is only 0.21 μH, confirming the decoupling of the two Tx coils. To maintain identical total wire lengths for both Design-1 and Design-2, Design-1 was wound with 5 turns and Design-2 with 1 turn. Litz wire, featuring

TABLE IV
MAIN PARAMETERS OF THE SYSTEM IN EXPERIMENT

Parameter	Value	Parameter	Value	Parameter	Value
L_{f1}	7.82 μH	L_{f2}	7.79 μH	L_{t1}(Design-1)	30.81 μH
L_{t2}(Design-1)	30.27 μH	L_{t1}(Design-2)	19.24 μH	L_{t2}(Design-2)	19.98 μH
M_3(Design-1)	0.61 μH	M_3(Design-2)	0.21 μH	L_s	37.64 μH
f_0 = 200 kHz					
Parameter	Value	Parameter	Value	Parameter	Value
Q_{t1}(Design-1)	297	Q_{t2}(Design-1)	301	Q_{t1}(Design-2)	256
Q_{t2}(Design-2)	261	Q_s	495		
f_0 = 401 kHz					
Parameter	Value	Parameter	Value	Parameter	Value
Q_{t1}(Design-1)	435	Q_{t2}(Design-1)	457	Q_{t1}(Design-2)	443
Q_{t2}(Design-2)	451	Q_s	610		

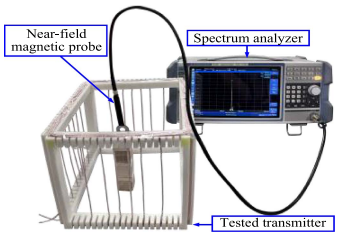

Fig. 20. Experimental setup for measuring the magnetic flux densities.

a diameter of 0.04 mm and comprising 1400 strands, is used for both Tx and Rx coils. The Tx framework consisted of 3D-printed cubic containers made of epoxy resin. The Rx coil, wound with 14 turns on both sides of a 10 mm thick wooden plate, is positioned at the mid-height of the container. The dc power supplies employed are Wanpteck S3010B. Primary-side GaN E-HEMT full-bridge inverters GS61004B-EVBCD are used. The switching signals for the two inverters are generated using a digital signal processor (DSP) TMS320F28335. The phase difference between the output voltage of the inverters is set to 90° in the DSP. The resistance of the load is regulated through a KIKUSUI PLZ405W electronic load. A diode bridge rectifier is implemented using four Schottky diodes PDS5100H-13. Main waveforms are captured using an eight-channel oscilloscope (Tektronix MSO58B). The input dc voltage to the system is 20 V. Two operating resonant frequencies, 200 kHz and 401 kHz, are tested separately. A rotating platform enabled the Rx to self-rotate or revolve. To mitigate potential interference between the rotating platform and the system, the cubic container is elevated on wooden legs and positioned 50 mm away from the rotating platform.

A. Magnetic Field Distribution Inside the Containers

The experimental setup for measuring the magnetic field distribution inside the container is shown in Fig. 20. The magnetic flux densities are measured using a spectrum analyzer (Model: FPL1007) equipped with a near-field magnetic probe (Model: SinnoRally type II). The probe detects the magnetic fields and converts their strengths into electrical signals, which are measured by the spectrum analyzer. During the measurement, the excitation currents are set to a frequency of 200 kHz with an rms value of 0.5 A. The phase difference angle between the two excitation currents is 90°.

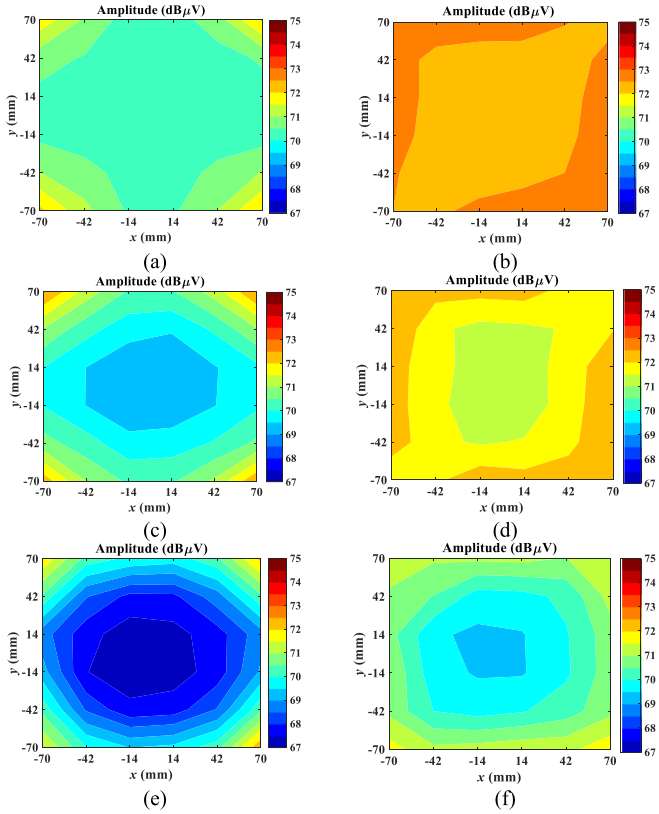

Fig. 21. Measured magnetic field distribution for the two designs. (a), (c), and (e) Measurement results for the layers at heights of 100 mm, 133 mm, and 166 mm for Design-1, respectively. (b), (d), and (f) Measurement results for the layers at heights of 100 mm, 133 mm, and 166 mm for Design-2, respectively.

TABLE V
AVERAGE AND COV VALUES OF THE MEASUREMENT RESULTS FOR THE TWO DESIGNS

	Design-1		Design-2	
	Avg. (dBμV)	CoV	Avg. (dBμV)	CoV
Height = 100 mm	70.61	0.0084	72.49	0.0038
Height = 133 mm	70.37	0.0137	71.89	0.0058
Height = 166 mm	69.16	0.0215	70.57	0.0101
Total	70.05	0.0178	71.65	0.0132

Measurements were conducted in three layers at heights of 100 mm, 133 mm, and 166 mm, respectively. Each layer employed a measurement area for both designs defined as {(x, y): -70 mm $\leq x \leq 70$ mm and -70 mm $\leq y \leq 70$ mm}, with a measurement step of 28 mm per point. At each measurement point, the probe was rotated from 0 to 180 degrees in 18-degree intervals, and the amplitudes of the sensed voltages are recorded by the spectrum analyzer. The average values of the sensed voltage across all degrees for both designs are presented in Fig. 21. Additionally, Table V lists the average and CoV values of the sensed voltages for both designs.

Evidently, the proposed design exhibits a more robust and evenly distributed magnetic field compared to the conventional design. Across the three layers, the average sensed voltage in the proposed design increases by 2.28% relative to the conventional

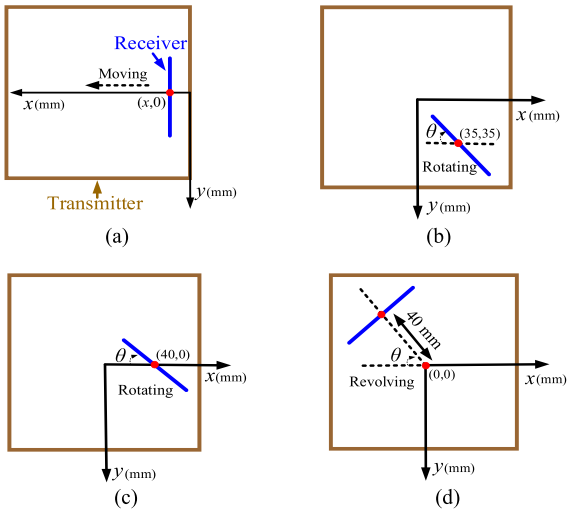

Fig. 22. Top views depicting the relative positions between the Tx and Rx for (a) Scenario-1, (b) Scenario-2, (c) Scenario-3, and (d) Scenario-4.

TABLE VI
COMPARISONS OF THE MEAN VALUE AND DEVIATION δ_{M} OF M_{EQ}

	Mean (μH)		δ_{M} (%)	
	Design-1	Design-2	Design-1	Design-2
Scenario-1	2.39	2.31	42.4	1.75
Scenario-2	2.11	2.38	19.17	17.97
Scenario-3	2.03	2.35	24.48	6.18
Scenario-4	2.17	2.44	22.45	11.57

design. Furthermore, the average CoV for the proposed design is reduced by 25.84% compared to the conventional design.

B. Comprehensive System Performance Evaluation

To assess the overall performance of the WPT system shown in Fig. 18, four scenarios involving varying movements of the Rx are tested. Fig. 22 illustrates the top views of the scenarios. In Scenario-1, the Rx coil is oriented horizontally along the y-direction and moves linearly along the x-direction. Scenarios-2 and -3 involve the Rx coil self-rotating at coordinates (35, 35) and (40, 0), respectively. In Scenario-4, the Rx coil revolves around the central point (0, 0) at a distance of 40 mm.

According to theoretical analysis, the output voltage and maximum efficiency are dependent on the equivalent mutual inductance M_{eq}, which is calculated from M_1 and M_2. The mutual inductances M_1 and M_2 for the two designs under the four scenarios were measured using a chemical impedance analyzer (model: Hioki IM3590), as presented in Fig. 23.

The deviation of the equivalent mutual inductance M_{eq} is defined as

$$\delta_{\mathrm{M}} = \frac{\delta_{\mathrm{M\_max}} - \delta_{\mathrm{M\_min}}}{\delta_{\mathrm{M\_min}}} \times 100\%. \tag{18}$$

The comparisons of the mean value and deviation δ_{M} of M_{eq} for the two designs across the four scenarios are listed in Table VI. The proposed design consistently exhibits a smaller δ_{M} for all scenarios, particularly in Scenario-1, Scenario-3, and Scenario-4, where δ_{M} is reduced by 24.11, 3.96, and 1.73 times,

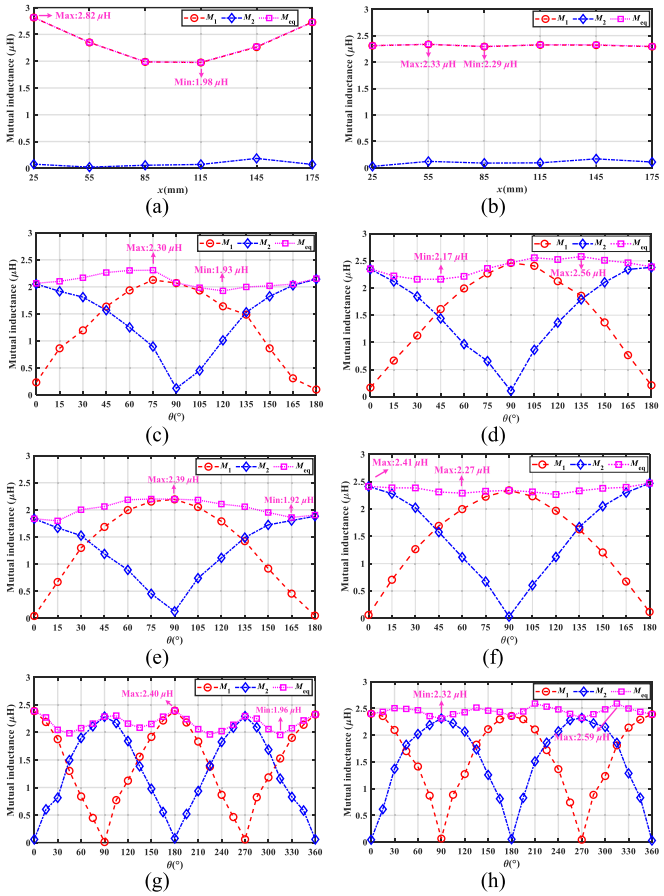

Fig. 23. Mutual inductances of the two designs under various Rx movements. Panels (a), (c), (e), and (g) correspond to Design-1 for Scenarios 1 to 4, respectively. Panels (b), (d), (f), and (h) correspond to Design-2 for Scenarios 1 to 4, respectively.

respectively. Moreover, the mean value of M_{eq} for Design-2 exceeds that of Design-1 in Scenario-2, Scenario-3, and Scenario-4. Therefore, the proposed design ensures more efficient energy transfer and reduced output fluctuations.

The performance of the system operating at 200 kHz is initially tested with a load resistance set to 5 Ω. The waveforms of v_{p1}, v_{p2}, i_{p1}, i_{p2}, i_{t1}, i_{t2}, i_{s}, and v_{s} for both designs with the Rx positioned in Scenario-2 at $\theta = 135°$ are displayed in Fig. 24. According to (16.1) and (16.2), when $M_1 = M_2$, the rms values of i_{p1} and i_{p2} are nearly identical, resembling the decoupled structure of the two Txs. Although the harmonics in i_{p1} and i_{p2} are high, they are irrelevant to the rotational control method. Instead, the excitation currents (i.e., i_{t1} and i_{t2}) are critical since they generate magnetic fields to excite Rx. The implementation of rotational method is to set a 90-degree phase difference between i_{t1} and i_{t2}, which can be achieved by setting a 90-degree phase difference between the output voltages of the inverters. As shown in Fig. 24, i_{t1} and i_{t2} exhibit similar rms values and a phase difference angle of 90°. As per (9) and the M_{eq} values calculated in Figs. 23(c) and (d), the rms value of i_{s} for Design-2 exceeds that of Design-1.

To evaluate the angular misalignment tolerance of the systems, a rotating platform is employed, allowing the Rx coil to

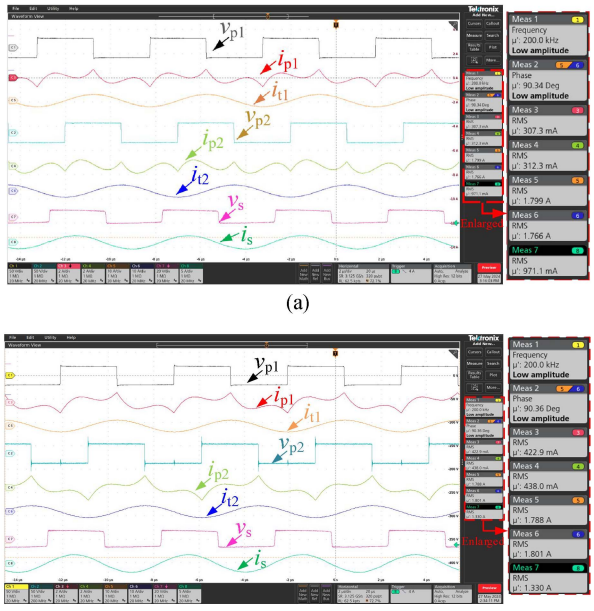

Fig. 24. Experimental waveforms for (a) Design-1 and (b) Design-2 at the operating frequency of 200 kHz.

TABLE VII
COMPARISONS OF THE MEAN AND DEVIATION δ_V OF V_o

	Mean (V)		δ_V (%)	
	Design-1	Design-2	Design-1	Design-2
Scenario-1	5.50	5.33	42.86	3.56
Scenario-2	4.63	5.25	16.86	15.40
Scenario-3	4.77	5.33	18.27	9.00
Scenario-4	4.91	5.52	27.37	13.50

self-rotate or revolve for Scenario-2, Scenario-3, and Scenario-4. The rotating platform completes one full rotation in 36 s. In Scenario-2 and Scenario-3, the Rx coil self-rotates 180° in 18 s. Another platform, capable of x-axis movement, tests dynamic performance for Scenario-1, covering 200 mm in 2 s. Fig. 25 illustrates the experimental waveforms of i_{p1}, i_{p2}, i_{t1}, i_{t2}, the output dc voltage V_o, and the output dc current I_o for both designs across Rx movements in the four scenarios. Here, V_{omin} and V_{omax} denote the minimum and maximum V_o observed during movement.

From Fig. 25, it is evident that i_{p1} and i_{p2} values fluctuate with movement of the Rx coil, whereas the excitation currents i_{t1} and i_{t2} remain consistent. The output voltage variations follow a trend similar to the calculated M_{eq}, as shown in Fig. 23. Furthermore, deviations in output voltage V_o are more pronounced in Design-1 compared to Design-2 across all four scenarios. The deviation of the output voltage V_o is defined as

$$\delta_V = \frac{V_{o\_max} - V_{o\_min}}{V_{o\_min}} \times 100\% . \tag{19}$$

The comparisons of the mean value and deviation δ_V of V_o for both designs across the four scenarios are listed in Table VII. Obviously, the proposed design reduces the deviation of V_o in all scenarios, particularly in Scenario-1, Scenario-3, and Scenario-4, where the deviation of V_o decreases by 12.04, 2.03, and 2.07 times, respectively. Furthermore, the average output voltage for Design-2 exceeds that of Design-1 in Scenario-2, Scenario-3, and Scenario-4.

TABLE VIII
COMPARISONS OF $\delta\eta$ BETWEEN THE TWO DESIGNS

	δ_η			
	Design-1 200 kHz	Design-2 200 kHz	Design-1 401 kHz	Design-2 401 kHz
Scenario-1	14.19%	1.93%	14.18%	1.21%
Scenario-2	4.40%	3.76%	4.83%	4.63%
Scenario-3	6.69%	2.28%	10.78%	1.29%
Scenario-4	7.01%	4.89%	6.01%	4.70%

To investigate the impact of quality factors and M_{eq} on maximum efficiency, the operating resonant frequency of the system is increased to 401 kHz. As shown in Table III, both Tx and Rx quality factors notably increased. Fig. 26 displays the main waveforms with the Rx coil positioned as in Fig. 24. Similarly, the rms values of i_{p1} and i_{p2} remain nearly unchanged. According to (6), the rms values of i_{t1} and i_{t2} decrease to approximately half of their values at 200 kHz. However, according to (8), increasing the resonant frequency does not affect the output voltage. Consequently, the rms values of i_s in Fig. 26 are similar to those in Fig. 24.

To determine the maximum efficiency, the initial load resistance is set to 1 Ω and incrementally increased in 0.5 Ω intervals. The dc–dc efficiency is measured at each load resistance value, and the maximum efficiencies for both designs across the four scenarios are plotted in Fig. 27.

As depicted in Fig. 27, increasing the quality factors of the coils leads to an approximate 10% rise in maximum efficiency. Moreover, the proposed Tx design consistently achieves higher maximum efficiency across most scenarios. Notably, in Scenario-3, the maximum efficiency of the proposed design consistently surpasses that of the conventional design. Furthermore, the proposed design ensures less variation in maximum efficiency. The deviation of the maximum efficiency, denoted as δ_η, is defined as

$$\delta_\eta = \frac{\delta_{\eta\max\_max} - \delta_{\eta\max\_min}}{\delta_{\eta\max\_min}} \times 100\% . \tag{20}$$

As shown in Table VIII, the proposed design markedly reduces the deviation of δ_η across systems with varying quality factors in the four scenarios. For Design-1, the deviation exceeds 10% in Scenario-1 and 5% in Scenario-3 and Scenario-4. In contrast, the deviation of δ_η for Design-2 is less than 5% across all scenarios, dropping below 3% in Scenario-3 and 2% in Scenario-1.

A detailed loss analysis for the proposed design with two specific Rx placements is presented in Fig. 28. The primary losses are distributed across the two inverters (i.e., P_{inv}), the transmitter coils (i.e., P_{Tx}), the receiver coil (i.e., P_{Rx}), and the diode-bridge rectifier (i.e., P_{rec}). The main losses occur in the rectifier and inverters. Notably, the rectifier accounts for over 45% of the losses, while the inverters contribute more than 23%. For the resonators, the losses in the Rx are lower than those in the Tx at an operating frequency of 200 kHz, whereas the losses in the Rx are higher than those in the Tx at 401 kHz.

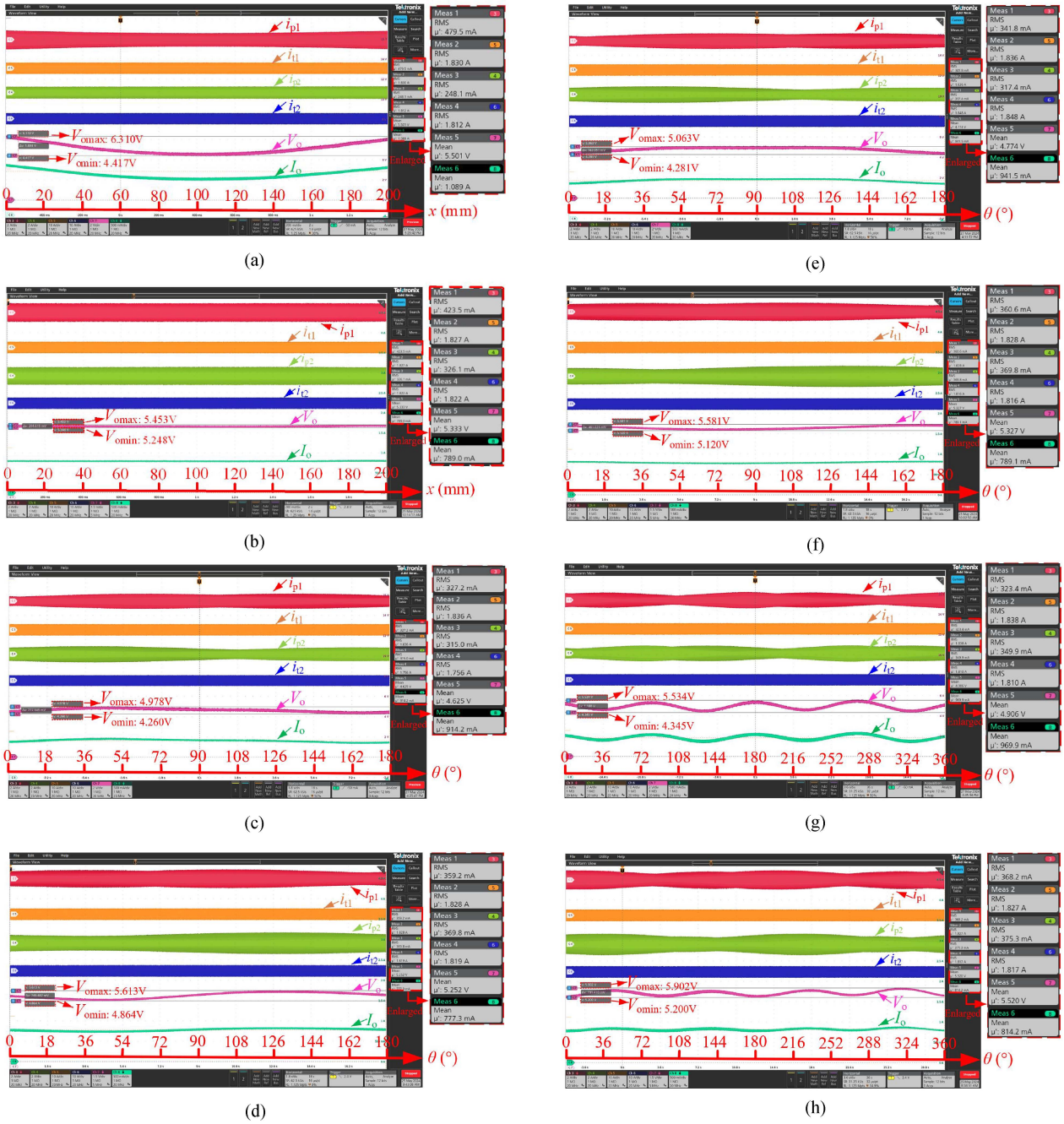

Fig. 25. Dynamic waveforms of i_{p1}, i_{p2}, i_{t1}, i_{t2}, V_o, and I_o for both designs. (a), (c), (e), and (g) correspond to Design-1 for Scenarios 1 to 4, respectively. (b), (d), (f), and (h) correspond to Design-2 for Scenarios 1 to 4, respectively.

C. Evaluation of Magnetic Field Exposure and Shielding Materials

According to the 2020 guidelines from the International Commission on Nonionizing Radiation Protection (ICNIRP) on limiting exposure to electromagnetic fields, the reference level of magnetic flux density in 200 kHz for local exposure of the general public, averaged over 6 min, should lower than 30.79 μT [43]. The magnetic field exposure of the proposed Tx is measured using a Hioki FT3470-50 magnetic field meter. The input dc voltage is set to 20 V, consistent with the experimental conditions. Five measurement points are tested, as shown in the Fig. 29(a). Points 1 to 4 are located outside with a distance d from the Tx, while point 5 is at the center of the Tx. To evaluate the shielding effects on the proposed system, a ferrite shielding plate (material PC95, 2 mm thick) and an aluminum shielding plate (0.5 mm thick) are placed on the outer surface of the Tx, as illustrated in Fig. 29(b).

The measurement results of the magnetic flux density are shown in Fig. 30. The measured value is approximately 34.5 μT for points 1 to 4 with d is 10 mm, which exceeds the ICNIRP boundary. However, when d increases to 20 mm, the magnetic

TABLE IX
COMPARISON OF KEY FEATURES AMONG EXISTING SPATIAL WPT SYSTEMS

Reference	Transmitter structure	Magnetic field characteristics	Operating frequency	Size of Tx/Rx	Power	Efficiency	Magnetic field uniformity considered?
[6]	Three orthogonal square coils	3-D target	19.56 kHz	32.8×32.8×32.8 cm /Φ27.6×1.1 cm	13.7 W	28.2%	No
[10]	Bowl-shaped with three sets of coils	3-D rotational	6.78 MHz	Not applicable /6.5×0.5 cm	5 W	68~80%	Yes
[12]	Cylindrical with three tubular coils	2-D rotational	100 kHz	Φ50×50 cm /10×10 cm	11 W	62%	Yes
[18]	Cubic with single coil	2-D	13.56 MHz	20×20×20 cm /20×20 cm	10 W	60%	No
[20]	Cubic with 12 magnetic dipoles	2-D	85 kHz	23×23×23 cm /not applicable	10 W	50%	Yes
[29]	Cubic with conventional folded coil	2-D	100 kHz	100×100×100 cm /Φ26×2 cm	1 W	10%	Yes
This work	Cubic with two multiple U-shaped folded coils	2-D rotational	200 kHz and 401 kHz	20×20×20 cm /Φ10×1 cm	10 W	60–72%	Yes

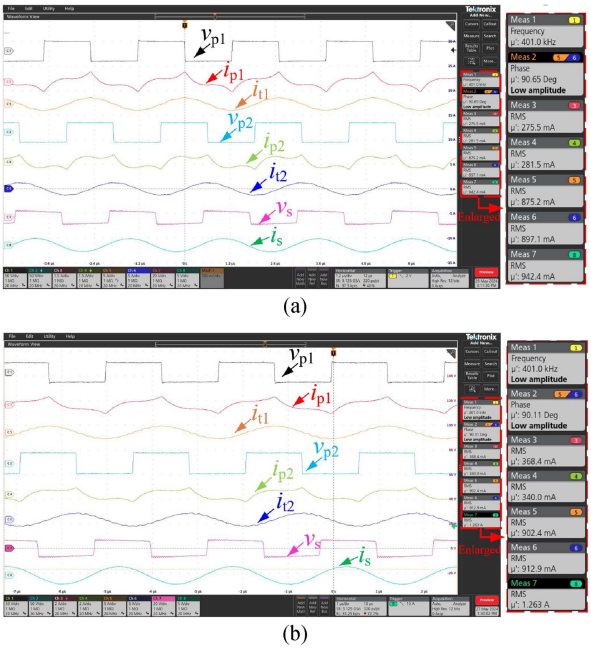

Fig. 26. Experimental waveforms of v_{p1}, v_{p2}, i_{p1}, i_{p2}, i_{t1}, i_{t2}, i_s, and v_s for Design-1 and (b) Design-2 at the operating frequency of 401 kHz.

flux density decreases to 29.2 μT, satisfying the standard. With the application of the ferrite shielding plate on the outer surface of the Tx, the magnetic flux density at points 1 to 4 is reduced to 7.2 μT, while the value at point 5 increases from 43.2 μT to 83.4 μT. When both ferrite and aluminum shielding materials are applied, the value at points 1 to 4 drops further to 0.49 μT, and the value reaches 80.4 μT at point 5. It should be noted that the shielding materials also affect the internal magnetic field distribution, and the parameters of the proposed Tx may need to be redesigned to account for this effect.

Table IX compares the key features among the existing spatial WPT systems. A rotational magnetic field involves the Tx generating magnetic flux that rotates regardless of load position, while a target magnetic field directs the flux toward the load. In this article, the magnetic field direction is controlled using the rotational method, eliminating the need for receiver position detection and complex current vector control strategies. In [18], [20], and [29], there is no phase difference in the current across the Tx coil, limiting the position and orientation of the receiver coil. In [12], three inverters are required to generate a 2-D rotational magnetic field. In this work, two inverters are used in two sets of Tx coils, achieving a true omnidirectional 2-D WPT. Additionally, the Tx coil structure is particularly designed to provide a highly uniform magnetic field distribution, ensuring stable power output.

VI. CONCLUSION

In this article, a spatial WPT system featuring of a novel cubic wireless charging Tx is proposed. The Tx coils are wound using only two wires. Compared to conventional cubic Tx designs, the proposed structure significantly enhances the uniformity of magnetic field distribution. Despite using a similar length of wire for the Tx coils, the new design improves the average magnetic flux density. The symmetry of the structure and rotational current control method ensure decoupling between the two Tx coils.

Based on the coil structures, a comprehensive circuit analysis of the spatial WPT system is also presented. The study investigates several key factors: 1) the impact of equivalent mutual inductance on output voltage stability, 2) the impact of equivalent mutual inductance on energy efficiency, 3) the cross-coupling effects of the Tx on inverter output current imbalance, and 4) the influence of quality factors on maximum efficiency. The parameters of the Tx coils are optimized by a meta-heuristic algorithm.

Experimental measurements using a spectrum analyzer confirm that our design achieves a more uniform magnetic field distribution. Additionally, a complete system is constructed and tested under four scenarios involving different movements of the Rx and two different frequencies, i.e., 200 kHz and 401 kHz. The results indicate that both the output voltage and overall efficiency (from dc to dc) of the spatial WPT systems with the proposed cubic Tx exhibit smaller deviations compared to systems with the conventional cubic Tx in all cases. Additionally, the average efficiency of the proposed systems operating at 401 kHz is 10% higher than that of the systems operating at 200 kHz.

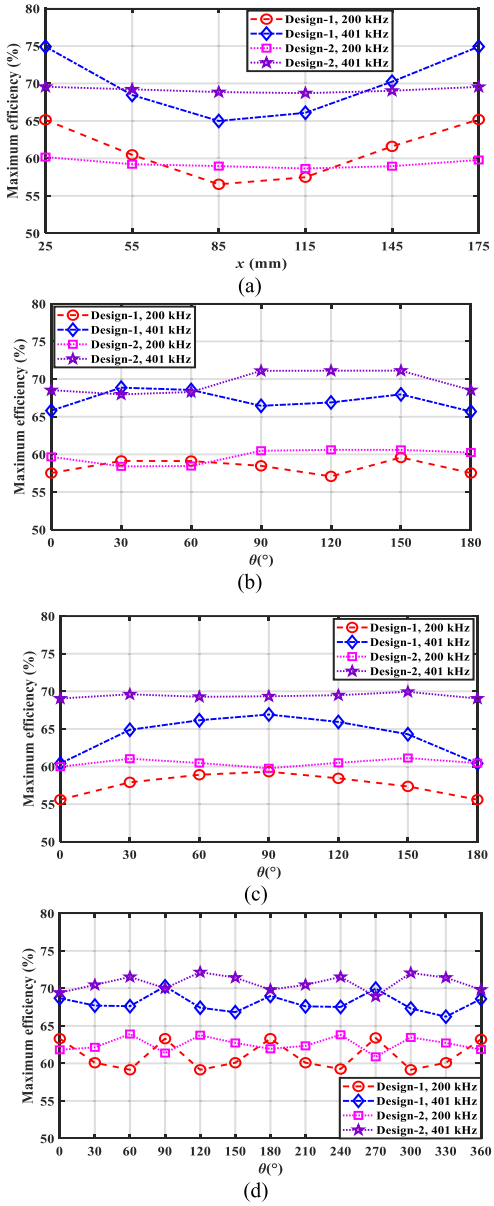

Fig. 27. Maximum efficiency for the two designs operating at two resonant frequencies in (a) Scenario-1, (b) Scenario-2, (c) Scenario-3, and (d) Scenario-4.

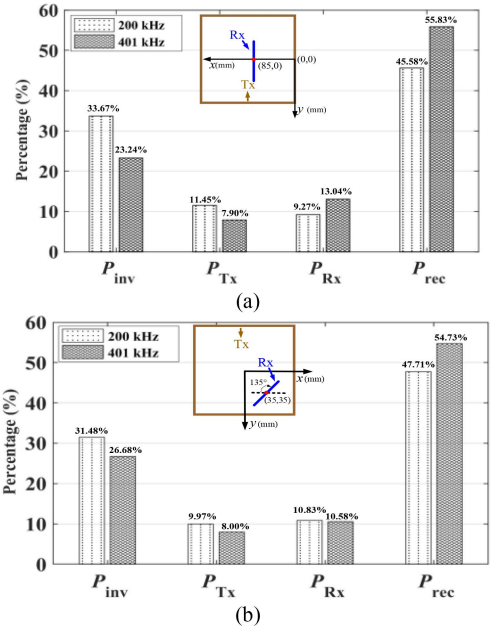

Fig. 28. Loss breakdown of the proposed design operating at two resonant frequencies in (a) Scenario-1 and (b) Scenario-2.

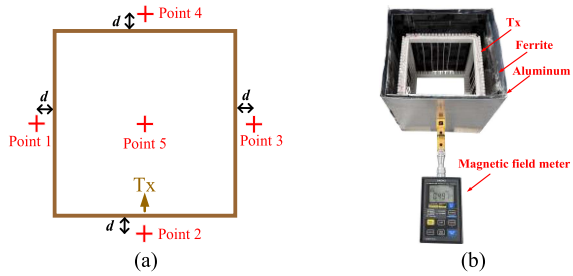

Fig. 29. Schematic diagrams of the measurements for magnetic field exposure. (a) Locations of the measurements. (b) Applied shielding plates.

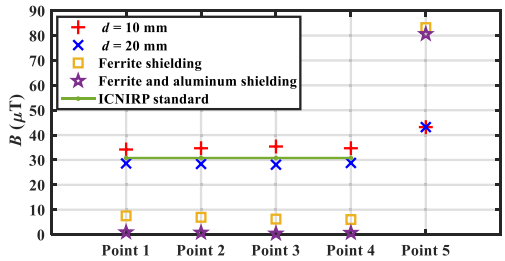

Fig. 30. Measured magnetic flux densities at different test points.

APPENDIX

According to Biot–Savart's law, the magnetic flux density $\vec{B}$ at an arbitrary point P (x_0, y_0, z_0) due to a current element $I\,d\vec{L}$ located at (x, y, z) can be expressed as

$$\vec{B} = \frac{\mu_0 I}{4\pi} \int \frac{d\vec{L} \times \vec{r}}{r^3} \tag{21}$$

where μ_0 is the vacuum permeability, I is the current in the coil, and $\vec{r}$ is the vector from point P to the current element (i.e., $\vec{r} = (x_0 - x, y_0 - y, z_0 - z)$). The magnetic field density $\vec{B}$ can be decomposed orthogonally into components along the x-, y-, and z-axes, denoted as B_x, B_y, and B_z, respectively. In the proposed design, focusing on the components B_x and B_y along the x- and y-axes direction, they can be expressed as

$$\begin{cases} B_x = \frac{\mu_0 I}{4\pi} \left(\int_{y_1}^{y_2} \frac{z_0 - z}{r^3} dy - \int_{z_1}^{z_2} \frac{y_0 - y}{r^3} dz \right) \\ B_y = \frac{\mu_0 I}{4\pi} \left(\int_{z_1}^{z_2} \frac{x_0 - x}{r^3} dz - \int_{x_1}^{x_2} \frac{z_0 - z}{r^3} dx \right) \end{cases}. \tag{22}$$

According to the vector superposition principle of magnetic fields, the magnetic flux densities B_x and B_y along the x- and y-axes, respectively, and the resultant $\vec{B}$, can be expressed as

$$\vec{B} = \vec{B_x} + \vec{B_y}\,. \tag{23}$$

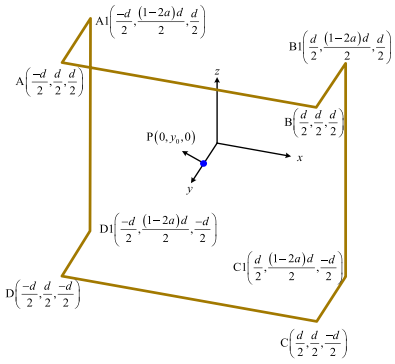

Fig. 31. Physical positions in an example coil.

To simplify the analysis, a folded coil positioned along the positive *y*-axis is considered. The schematic diagram illustrating the coil's position is shown in Fig. 31. The coordinates of an arbitrary point on the coil can be expressed as

$$\begin{aligned}
&(\mathrm{A},\mathrm{A1}): x=-\frac{d}{2}, y\in\left[\frac{d}{2},\frac{(1-2\alpha)\,d}{2}\right], z=\frac{d}{2}\\
&(\mathrm{A1},\mathrm{D1}): x=-\frac{d}{2}, y=\frac{(1-2\alpha)\,d}{2}, z\in\left[\frac{d}{2},-\frac{d}{2}\right]\\
&(\mathrm{D1},\mathrm{D}): x=-\frac{d}{2}, y\in\left[\frac{(1-2\alpha)\,d}{2},\frac{d}{2}\right], z=-\frac{d}{2}\\
&(\mathrm{D},\mathrm{C}): x\in\left[-\frac{d}{2},\frac{d}{2}\right], y=\frac{d}{2}, z=-\frac{d}{2}\\
&(\mathrm{C},\mathrm{C1}): x=\frac{d}{2}, y\in\left[\frac{d}{2},\frac{(1-2\alpha)\,d}{2}\right], z=-\frac{d}{2}\\
&(\mathrm{C1},\mathrm{B1}): x=\frac{d}{2}, y=\frac{(1-2\alpha)\,d}{2}, z\in\left[-\frac{d}{2},\frac{d}{2}\right]\\
&(\mathrm{B1},\mathrm{B}): x=\frac{d}{2}, y\in\left[\frac{(1-2\alpha)\,d}{2},\frac{d}{2}\right], z=\frac{d}{2}\\
&(\mathrm{B},\mathrm{A}): x=\in\left[\frac{d}{2},-\frac{d}{2}\right], y=\frac{d}{2}, z=\frac{d}{2}
\end{aligned}\tag{24}$$

where α represents the folded ratio defined as $\alpha = l/d$. The point P is situated on the *y*-axis for simplification. By substituting (22) into (21), The amplitude of the magnetic field at point P can be computed as

$$B = \frac{\mu_0 I d^2}{4\pi}\left(\frac{1}{\sqrt{\left(\frac{d^2}{2}+\left|y_0+d\left(\alpha-\frac{1}{2}\right)\right|^2\right)^3}} + \frac{1}{\sqrt{\left(\frac{d^2}{2}+\left|\frac{d}{2}-y_0\right|^2\right)^3}}\right).\tag{25}$$

From (25), it is evident that the amplitude of the magnetic field at points on the *y*-axis depends on both the folded ratio and the position. For instance, considering two points, i.e., $P1(0,0,0)$ and $P2(0,d/2,0)$, the CoV can be calculated as follows

$$\mathrm{CoV} \approx \frac{|-0.06-\beta_1+\beta_2|}{1.48+\beta_1+\beta_2}\tag{26}$$

where β_1 and β_2 can be expressed as

$$\begin{cases}\beta_1 = \frac{4}{\sqrt{(4\alpha^2-4\alpha+3)^3}}\\ \beta_2 = \frac{\sqrt{2}}{2\sqrt{(2\alpha^2+1)^3}}.\end{cases}\tag{27}$$

Deriving the analytical solution for the optimal value of α, as indicated by (26) and (27), proves challenging. It is crucial to acknowledge that the complexity of CoV expression escalates notably when incorporating numerous folded coils and arbitrary test points. Furthermore, achieving a more accurate representation of the magnetic field distribution necessitates sampling a large number of points. For instance, this study evaluated 753 571 points, rendering the derivation of an analytical solution for α unfeasible.

REFERENCES

[1] S. Y. R. Hui, Y. Yang, and C. Zhang, "Wireless power transfer: A paradigm shift for the next generation," *IEEE J. Emerg. Sel. Topics Power Electron.*, vol. 11, no. 3, pp. 2412–2427, Jun. 2023.

[2] S. Y. R. Hui, "Planar wireless charging technology for portable electronic products and Qi," *Proc. IEEE*, vol. 101, no. 6, pp. 1290–1301, Jun. 2013.

[3] H. Zhang, S. Gao, T. Ngo, W. Wu, and Y. Guo, "Wireless power transfer antenna alignment using intermodulation for two-tone powered implantable medical devices," *IEEE Trans. Microw. Theory Techn.*, vol. 67, no. 5, pp. 1708–1716, May 2019.

[4] H. Liu et al., "Dynamic wireless charging for inspection robots based on decentralized energy pickup structure," *IEEE Trans. Ind. Inform.*, vol. 14, no. 4, pp. 1786–1797, Apr. 2018.

[5] Z. Zhang and B. Zhang, "Angular-misalignment insensitive omnidirectional wireless power transfer," *IEEE Trans. Ind. Electron.*, vol. 67, no. 4, pp. 2755–2764, Apr. 2020.

[6] Q. Zhu, M. Su, Y. Sun, W. Tang, and A. P. Hu, "Field orientation based on current amplitude and phase angle control for wireless power transfer," *IEEE Trans. Ind. Electron.*, vol. 65, no. 6, pp. 4758–4770, Jun. 2018.

[7] C. Zhang, D. Lin, and S. Hui, "Basic control principles of omnidirectional wireless power transfer," *IEEE Trans. Power Electron.*, vol. 31, no. 7, pp. 5215–5227, Jul. 2016.

[8] W. M. Ng, C. Zhang, D. Lin, and S. Hui, "Two- and three-dimensional omnidirectional wireless power transfer," *IEEE Trans. Power Electron.*, vol. 29, no. 9, pp. 4470–4474, Sep. 2014.

[9] J. Feng, Q. Li, and F. Lee, "Coil and circuit design of omnidirectional wireless power transfer system for portable device application," in *Proc. Eur. Conf. Cogn. Ergon*, Sep. 2018, pp. 914–920.

[10] J. Feng, Q. Li, F. C. Lee, and M. Fu, "Transmitter coils design for free-positioning omnidirectional wireless power transfer system," *IEEE Trans. Ind. Inform.*, vol. 15, no. 8, pp. 4656–4664, Aug. 2019.

[11] H. Zhuang, W. Wang, and G. Yan, "Omnidirectional wireless power transfer system using modified saddle-shaped coil pair for implantable capsule robots," *IEEE Trans. Power Electron.*, vol. 38, no. 9, pp. 11664–11672, Sep. 2023.

[12] T. Feng, Y. Sun, Z. Zuo, Z. Wang, and X. Dai, "Magnetic field analysis and excitation currents optimization for an omnidirectional WPT system based on three-phase tubular coils," *IEEE Trans. Ind. Appl.*, vol. 58, no. 1, pp. 1268–1278, Jan./Feb. 2022.

[13] T. Sasatani, A. P. Sample, and Y. Kawahara, "Room-scale magnetoquasistatic wireless power transfer using a cavity-based multimode resonator," *Nature Electron.*, vol. 4, no. 9, pp. 689–697, Aug. 2021.

[14] K. Wang, R. Liang, Z. Sun, and Y. Yang, "Multiple folding coils design for octagonal prism-based wireless charging container with even magnetic flux density distribution," in *Proc. Wireless Power Technol. Conf. Expo.*, May 2024, pp. 1–6.

[15] J. Hourtoule, D. van Houtte, P. Fejoz, and P. Hertout, "Magnetic compatibility of standard components for electrical installations: Tests on programmable logical controllers and other electronic devices," *Fusion Eng. Des.*, vol. 75–79, no. 11, pp. 179–183, 2005.

[16] S. Wang, Y. Lu, Y. Yang, and Q. Jiang, "Analysis and test of a 1m/275mT large-scale high-intensity magnetic field immunity test coil system for ITER," *Fusion Eng. Des.*, vol. 188, Mar. 2023, Art. no. 113405.
[17] IEC Standard 61000-4-8, "Electromagnetic Compatibility (EMC)—Part 4-8: Testing and measurement techniques—Power frequency magnetic field immunity test," IEC, 2009.
[18] N. Ha-Van and C. Seo, "Analytical and experimental investigations of omnidirectional wireless power transfer using a cubic transmitter," *IEEE Trans. Ind. Electron.*, vol. 65, no. 2, pp. 1358–1366, Feb. 2018.
[19] C. Rong et al., "Omnidirectional free-degree wireless power transfer system based on magnetic dipole coils for multiple receivers," *IEEE Access*, vol. 9, pp. 81588–81600, 2021.
[20] C. Rong, X. He, Y. Zeng, C. Lu, and M. Liu, "High-efficiency orientation insensitive WPT systems using magnetic dipole coil for low-power devices," *IEEE Trans. Power Electron.*, vol. 37, no. 5, pp. 4985–4990, May 2022.
[21] Z. Jia, G. Yan, Z. Wang, and H. Liu, "Efficiency optimization of wireless power transmission systems for active capsule endoscopes," *Physiol. Meas.*, vol. 32, no. 10, pp. 1561–1573, Aug. 2011.
[22] J. Gao et al., "Stable wireless power transmission for a capsule robot with randomly changing attitude," *IEEE Trans. Power Electron.*, vol. 38, no. 2, pp. 2782–2796, Feb. 2023.
[23] A. Jodko-Władzińska, K. Wildner, T. Pałko, and M. Władziński, "Compensation system for biomagnetic measurements with optically pumped magnetometers inside a magnetically shielded room," *Sensors*, vol. 20, no. 16, Aug. 2020, Art. no. 4563.
[24] F. Fiorillo, *Characterization and Measurement of Magnetic Materials*. Cambridge, MA, USA: Academic, 2004.
[25] J. D. Spencer and R. Davis, "Helmholtz coils for MIL-STD-462D RS101 testing," *IEEE Int. Symp. Electromagn. Compatability*, vol. 2, pp. 940–942, Aug. 1999, doi: 10.1109/ISEMC.1999.810184.
[26] M. R. Basar, M. Y. Ahmad, J. Cho, and F. Ibrahim, "Stable and high-efficiency wireless power transfer system for robotic capsule using a modified Helmholtz coil," *IEEE Trans. Ind. Electron.*, vol. 64, no. 2, pp. 1113–1122, Feb. 2017.
[27] X. Deng et al., "High-uniformity calculation method of four-coil configuration in large-caliber magnetic field immunity testing system," *IEEE Trans. Plasma Sci.*, vol. 50, no. 6, pp. 1977–1987, Jun. 2022.
[28] Y. Huang, L. Jiang, P. Fu, Z. Huang, and X. Xu, "Optimal design method to improve the magnetic field distribution of multiple square coil systems," *IEEE Access*, vol. 8, pp. 171184–171194, 2020.
[29] K. Li, J. Wu, K. Wang, Y. Yang, Y. Tang, and S. Y. R. Hui, "A folded coil design for cubic wireless charging space frames with even magnetic flux density distribution," *IEEE Trans. Power Electron.*, vol. 39, no. 8, pp. 9040–9050, Aug. 2024.
[30] K. Wang, R. Liang, J. Gao, J. Wu, Y. Tang, and Y. Yang, "Optimized folded coil designs for wireless charging chambers with even distribution of magnetic flux density," in *Proc. IEEE Appl. Power Electron. Conf. Expo.*, 2024, pp. 2859–2863.
[31] K. Wang, R. Liang, Z. Sun, Y. Wang, and Y. Yang, "A comparative study on magnetic flux density distribution in wireless charging chambers using rotational method," in *Proc. IEEE Wireless Power Technol. Conf. Expo*, 2024, pp. 91–95.
[32] J. Sun, A. Diet, Y. L. Bihan, M. Biancheri-Astier, C. Gannouni, and M. Police, "Planar omnidirectional detection of RFID/NFC patches inside a cubic structure," *IEEE J. Radio Freq. Identification*, vol. 8, pp. 206–216, Apr. 2024, doi: 10.1109/JRFID.2024.3383609.
[33] C. Liang, H. Yuan, R. Zhang, A. Yang, X. Wang, and M. Rong, "Analysis and design of a novel cubic WPT system in a metal environment for an enclosed sensor scenario," *IET Power Electron.*, vol. 16, pp. 1305–1319, 2023.
[34] M. Milutinov, I. Sreckovic, A. Juhas, and N. Pekaric-Na, "Study on elliptically polarized magnetic field generated by two orthogonal Helmholtz coils," in *Proc. Int. Conf. Appl. Electromagnetics*, 2015, pp. 1–5.
[35] D. S. Batista, F. Granziera, M. C. Tosin, and L. F. de Melo, "Three-axial Helmholtz coil design and validation for aerospace applications," *IEEE Trans. Aerosp. Electron. Syst.*, vol. 54, no. 1, pp. 392–403, Feb. 2018.
[36] M. E. Rudd and J. R. Craig, "Optimum spacing of square and circular coil pairs," *Rev. Sci. Instrum.*, vol. 39, no. 9, pp. 1372–1374, Sep. 1968.
[37] K. Yang et al., "Calibration of SQUID magnetometers in multichannel MCG system based on bi-planar coil," *IEEE Trans. Instrum. Meas.*, vol. 71, Feb. 2022, Art. no. 1002209, doi: 10.1109/TIM.2022.3150588.
[38] Y. Lu, Y. Yang, M. Zhang, R. Wang, L. Jiang, and B. Qin, "Improved square-coil configurations for homogeneous magnetic field generation," *IEEE Trans. Ind. Electron.*, vol. 69, no. 6, pp. 6350–6360, Jun. 2022.
[39] J. Lu, S. Wang, F. Lu, C. Lu, X. Zhang, and D. Ma, "Hybrid optimal design of square highly uniform magnetic field coils," *IEEE Trans. Ind. Electron.*, vol. 70, no. 4, pp. 4236–4244, Apr. 2023.
[40] K. Amine, "Multiobjective simulated annealing: Principles and algorithm variants," *Adv. Operations Res.*, vol. 2019, 2019, Art. no. 8134674.
[41] S. Li, W. Li, J. Deng, T. D. Nguyen, and C. C. Mi, "A double-sided LCC compensation network and its tuning method for wireless power transfer," *IEEE Trans. Veh. Technol.*, vol. 64, no. 6, pp. 2261–2273, Jun. 2015.
[42] Y. Yang, "Precise modeling of nonlinear rectifier loads in wireless power transfer systems," *IEEE J. Emerg. Sel. Topics Power Electron.*, vol. 11, no. 3, pp. 3574–3585, Jun. 2023.
[43] "Guidelines for limiting exposure to electromagnetic fields (100 kHz to 300 GHz)," *Health Phys.*, vol. 118, no. 5, pp. 483–524, May 2020.

Kaiyuan Wang (Student Member, IEEE) received the B.Eng. degree from Northeast Electric Power University, Jilin City, China, in 2020, and the M.Phil. degree from The Hong Kong Polytechnic University, Hong Kong, in 2023, both in electrical engineering. He is currently working toward the Ph.D. degree in electrical engineering with Nanyang Technological University, Singapore.

His research interests include wireless power transfer and power electronics.

Zhen Sun (Student Member, IEEE) received the B.Eng. degree in electrical engineering from Tsinghua University, Beijing, China, in 2023. She is currently working toward the Ph.D. degree in electrical engineering with the Nanyang Technological University, Singapore.

Her research interests include power electronics and advanced control.

Xinze Li (Member, IEEE) received the B.Eng. degree in electrical engineering from Shandong University, Jinan, China, 2018, and the Ph.D. degree in electrical and electronic engineering from Nanyang Technological University, Singapore, in 2023.

He joined with the University of Arkansas, USA, as a Research Fellow in 2024. His research interests include power converter design and modulation design.

Yao Wang (Member, IEEE) received the B.Eng. and M.Eng. degrees from Northwestern Polytechnical University, Xi'an, China, in 2017 and 2020, respectively, and the Ph.D. degree from Drexel University, Philadelphia, PA, USA, in 2023, all in electrical engineering.

He is currently a Postdoctoral Research Fellow with Nanyang Technological University, Singapore. His research interest includes wireless power transfer.

Yun Yang (Senior Member, IEEE) received the B.Sc. degree from Wuhan University, Wuhan, China, in 2012, and the Ph.D. degree from The University of Hong Kong, Hong Kong, in 2017, both in electrical engineering.

He was a Research Assistant Professor with the Department of Electrical Engineering, The Hong Kong Polytechnic University. He is currently an Assistant Professor with the School of Electrical and Electronic Engineering, Nanyang Technological University. His research interests include power electronics, wireless power transfer, energy storage technologies, and smart grid systems.